Necrosis-induced apoptosis promotes regeneration in *Drosophila* wing imaginal discs

Jacob Klemm, Michael J. Stinchfield, Robin E. Harris

School of Life Sciences, Arizona State University, Tempe, AZ 85728

Running Title: Necrosis-induced wing disc regeneration

Keywords: regeneration, cell death**,** Drosophila, apoptosis, gene expression, necrosis, imaginal disc

Corresponding Author Details:

Robin Harris,

Arizona State University

427 E Tyler Mall LSE 229

Attn: Dr. Rob Harris, LSE 333

Tempe

AZ 85287-4501

Robin.Harris@ASU.edu

(480) 965 7543

Abstract

Regeneration is a complex process that requires a coordinated genetic response to tissue loss. Signals from dying cells are crucial to this process and are best understood in the context of regeneration following programmed cell death, like apoptosis. Conversely, regeneration following unregulated forms of death such as necrosis have yet to be fully explored. Here we have developed a method to investigate regeneration following necrosis using the *Drosophila* wing imaginal disc. We show that necrosis stimulates regeneration at an equivalent level to that of apoptosis-mediated cell death and activates a similar response at the wound edge involving localized JNK signaling. Unexpectedly however, necrosis also results in significant apoptosis far from the site of ablation, which we have termed necrosis-induced apoptosis (NiA). This apoptosis occurs independent of changes at the wound edge and importantly does not rely on JNK signaling. Furthermore, we find that blocking NiA limits proliferation and subsequently inhibits regeneration, suggesting that tissues damaged by necrosis can activate programmed cell death at a distance from the injury to promote regeneration.

Introduction

Apoptosis has a fundamental role in shaping organisms during development and in maintaining tissue homeostasis (Fuchs and Steller 2011; Suzanne and Steller 2013). This vital cellular process acts to counter infection, suppress tumor formation and promote recovery from damage (Fogarty and Bergmann 2017; Hacker 2018; Wong 2011). These events occur because dying cells release signals that act on surrounding cells, resulting in different outcomes depending on the nature of the signals and the tissue context (Fogarty and Bergmann 2015; Fuchs and Steller 2015; Perez-Garijo and Steller 2015; Su 2015). Numerous aspects of regeneration can be dependent on this apoptotic signaling, including morphogenesis, inflammation and tissue regrowth (Bergmann and Steller 2010; Perez-Garijo and Steller 2015; Vriz et al. 2014). In many organisms, factors released from dying cells stimulate the proliferation of adjacent cells as a replacement mechanism (Chera et al. 2009; Li et al. 2010; Pellettieri et al. 2010; Su 2015; Tseng et al. 2007; Vriz et al. 2014). This specialized form of compensatory proliferation is known as apoptosis-induced proliferation (AiP) (Fogarty and Bergmann 2017), in which a number of mitogens, including WNTs, TGFβ, EGF and Hedgehog, are released from dying cells (Fogarty and Bergmann 2017; Fuchs and Steller 2015). Upstream factors that lead to their production, such as JNK signaling and the activation of caspases, have also been described (Fogarty and Bergmann 2017; Pinal et al. 2019). Conversely, apoptosis can also promote the death of surrounding cells, a process known as apoptosis-induced apoptosis (AiA), (Fogarty and Bergmann 2015; Perez-Garijo et al. 2013; Su 2015). This process also relies on JNK signaling and possibly represents a mechanism to ensure the proper coordination of cell death across a tissue (Perez-Garijo et al. 2013). Signals from dying cells can also

58 result in non-autonomous protection from cell death, ensuring the preservation of
59 neighboring cells after injury (Bilak et al. 2014). Thus, cell death can strongly influence
60 the behavior of surrounding cells and consequently regulate the ability of a tissue to
61 recover from damage.
62
63 Evidence that signals from apoptotic cells impact surrounding tissues first originated from
64 studies of the *Drosophila* wing imaginal disc, a larval epithelial tissue that forms the adult
65 wing (Huh et al. 2004; Perez-Garijo et al. 2004; Ryoo et al. 2004). The wing disc has been
66 extensively characterized as a model for growth and development, and for its significant
67 capacity to regenerate (Beira and Paro 2016; Hariharan and Serras 2017; Worley et al.
68 2012). Much of our understanding of imaginal disc regeneration has derived from
69 GAL4/UAS-based genetic ablation tools, in which tissue-specific apoptosis is induced by
70 a temperature change, permitting the study of regeneration *in situ* (Fox et al. 2020).
71 However, these ablation tools rely on activating the apoptotic machinery to induce
72 damage, limiting our ability to explore other types of cell death. One example is necrosis,
73 the rapid and disordered death of a cell characterized by the loss of membrane integrity
74 and release of cytoplasmic contents into the surrounding tissue (Fuchs and Steller 2015).
75 Several factors released by cells undergoing necrosis have been identified and
76 characterized as signaling molecules that might influence the behavior of surviving
77 tissues (Bianchi 2007; Patel 2018; Venereau et al. 2015), although their role in wound
78 recovery and regeneration is currently not well understood. In humans, necrosis can
79 occur in all types of tissues and results from environmental insults like burns or frostbite,
80 microbial infection (Bonne and Kadri 2017; Hakkarainen et al. 2014), and from common

81 ischemic events such as heart attacks and strokes (Konstantinidis et al. 2012; Radak et
82 al. 2017; Yuan 2009). Various inherited and congenital conditions can also lead to
83 necrosis, including joint disorders and sickle cell anemia (Masi et al. 2007; Milner et al.
84 1991). Thus, a better understanding of how a tissue responds to damage could advance
85 therapeutic methods to improve healing and regeneration in many human disease and
86 injury contexts.
87
88 Here we have developed a method to induce necrotic cell death in the wing imaginal disc
89 and used it to characterize the genetic response to necrosis compared to apoptosis. Our
90 results show that wing discs can regenerate following necrosis but do so by inducing
91 extensive JNK-independent apoptosis at a distance from the site of injury. Importantly,
92 we demonstrate that this necrosis-induced apoptosis is required for localized proliferation
93 and efficient regeneration.

Materials and Methods

Drosophila stocks and crosses

Flies were cultured in conventional dextrose fly media at 25ºC at 12 hr light-dark cycles. The recipe for dextrose media contains 9.3 g agar, 32 g yeast, 61 g cornmeal, 129 g dextrose, and 14 g tego in 1 L distilled water. Complete fly line details and RRIDs are available in the Reagent Table. Genotypes for each figure panel are listed in the Supplemental Methods File. The lines used as ablation stocks are as follows: *hs-flp; hs-p65; R85E08-DBD, DVE>>GAL4* (*DC^{NA}), hs-flp ; lexAop-GluR1^{Lc8} , hs-p65 ; salm-LexADBD , DVE>>GAL4 / S-T* (*DC^{GluR1}), hs-flp ; lexAop-GluR1^{Lc}, hs-p65 / CyO ; salm-LexADBD / TM6C, sb* (*DC^{GluR1} no GAL4*), *hs-flp ; lexAop-hep^{CA} , hs-p65 ; R85E08-DBD, DVE>>GAL4/S-T* (*DC^{hepCA}*), and *hs-flp ; lexaOp-rpr , hs-p65 / CyO, salm-LexADBD , DVE>>GAL4* (*DC^{rpr}*,(Harris et al. 2020). The stock *DR^{WNT}-GFP* was used as a marker for early regeneration (Harris et al. 2016). The following stocks were obtained from Bloomington Drosophila Stock Center: *UAS-y^{RNAi}* (BL#64527), *UAS-p35* (BL#5073), *PCNA-GFP* (BL#25749), *UAS-bsk^{RNAi}* (BL#53310), *UAS-bsk^{DN}* (BL#9311), *UAS-egr^{RNAi}* (BL#58993), *puc^{A251}* (BL#11173), *hep^{r75}* (BL#6761), *UAS-hepCA* (BL#58981), *UAS-wg^{RNAi}* (BL#32994), *UAS-Mkk4^{RNAi}* (BL#35143), *UAS-hep^{RNAi}* (BL#28710), *UAS-rpr^{RNAi}* (51846), and *hid^{1}* (BL#631). *CyclinE-GFP* was a gift from the Wei Du lab. *UAS-grnd^{RNAi}* was a gift from the Bilder lab at UC Berkeley. *UAS-miRHG* and *UAS-nlsGFP; egr-GAL4* were gifts from the Hariharan lab at UC Berkeley. *UAS-GluR1^{Lc8}* (Liu et al. 2014) was a gift from the Xie lab at Stowers Institute.

Generation of *lexAOp-hep^{CA}*, *lexAOp-GluR1^{Lc8}*, and *DR^{WNT}-GAL80* lines

117 To generate *lexAop-hep^{CA}*, the coding region for *hep^{CA}* was cloned from *UAS-hep^{CA}* stock
118 and subcloned into the *lexAop-GFP* vector following excision of GFP, using XhoI and XbaI
119 sites. *LexAop-GluR1^{Lc8}* was generated by cloning out the *GluR1^{Lc8}* coding region from
120 *UAS-GluR1^{Lc8}* and subcloning it into the *lexAop-GFP* vector following excision of the *GFP*,
121 using *XhoI* and *XbaI* sites. The *lexAop-hep^{CA}* and *lexAop-GluR1^{Lc8}* constructs were
122 sequence verified and inserted into the Su(Hw)attP5 landing site via PhiC31 insertion.
123 To generate *DR^{WNT}-GAL80*, the GAL80 coding sequence was cloned from tub-GAL80
124 genomic DNA (BL#5132) and subcloned into the *DR^{WNT}-GFP* plasmid following excision
125 of the *GFP* (Harris et al. 2016), using *AgeI* and *XbaI* sites. *DR^{WNT}-GAL80* was sequence
126 verified and inserted into the *attp40* and *VK00027* landing sites via PhiC31 insertion.
127 Transgenic flies were generated by embryo injections performed by BestGene, Inc.
128

129 **Ablation Experiments**

130 DUAL Control experiments were performed essentially as described in (Harris et al.
131 2020). Experimental crosses were cultured at 25°C and density controlled at 50 larvae
132 per vial. Larvae were heat shocked at day 3.5 or 4.5 of development (84 and 108 hours
133 after egg lay (AEL), respectively) by placing vials in a 37°C water bath for 45 minutes,
134 followed by a return to 25°C. Larvae were allowed to recover for 18 hr before being
135 dissected, fixed and stained, unless otherwise indicated. The non-ablating version of
136 DUAL Control (*DC^{NA}*) was used as a control while *UAS-y^{RNAi}* was used as a control for
137 RNAi experiments. DUAL Control experiments utilized the *DVE>>GAL4* driver that drives
138 expression in the majority of the wing pouch (Figure S1A-B). In the experiment to examine

139 *egr* (Figure S4H-J), *egr-GAL4* was utilized instead of *DVE>>GAL4*, which drives in the
140 adult muscle precursor (AMP) cells of the disc (Everetts et al. 2021).
141
142 **Regeneration Scoring and Wing Measurements**
143 Wings of adult flies from heat shocked larvae were scored and measured after genotype
144 blinding by another researcher. Scoring was performed on anesthetized adults by binning
145 into a regeneration scoring category (Figure 1G and (Harris et al. 2020). Wing
146 measurements were performed by removing wings, mounting in Permount solution and
147 imaging using a Zeiss Discovery.V8 microscope. Wing area was measured using the
148 Image J software. Male and female adults were measured separately to account for sex
149 differences in wing size, using a reproducible measuring protocol that excludes the
150 variable hinge region of the wing (details of measuring protocol available on request).
151 Statistics were performed using GraphPad Prism 9.0.
152
153 **Immunohistochemistry**
154 Larvae were dissected in PBS followed by a 20-minute fix in 4% paraformaldehyde in
155 PBS. After 3 washes in 0.1% PBST (Triton-X), larvae were washed in 0.3% PBST and
156 then blocked in 0.1% PBST with 5% NGS for 30 minutes. Primary staining was done
157 overnight at 4°C, while secondary staining was done for 4 hours at room temperature.
158 The following primary antibodies were obtained from the Developmental Studies
159 Hybridoma Bank: mouse anti-Nubbin (1:25), mouse anti-Wg (1:100), mouse anti-Mmp1
160 C-terminus (1:100), mouse anti-Mmp1 catalytic domain (1:100), mouse anti-LacZ (1:100),
161 and rat anti-DE-Cadherin (1:100). Rabbit anti-Dcp1 (1:1000) and mouse anti-PH3 (1:400)

162 was obtained from Cell Signaling Technologies, and chick anti-GFP (1:2000) was
163 obtained from Abcam. The secondary anti-Chick 488 antibody was also obtained from
164 Abcam. Other secondary antibodies, anti-rabbit 647, anti-rat 647, and anti-mouse 555
165 were obtained from Invitrogen. All secondary fluorophore-conjugated antibodies were
166 used at 1:500. Images were obtained on a Zeiss AxioImager.M2 with ApoTome. For each
167 experiment at least 15 discs were analyzed prior to choosing a representative image.
168 Images were processed using Affinity Photo and Affinity Designer.
169

170 **Propidium Iodide staining and TUNEL Assay**

171 Propidium iodide (PI) staining was achieved by incubating freshly dissected wing imaginal
172 discs in Schneider's Media with 15 μM PI for 10 minutes, followed by several washes in
173 PBS and immediately mounting and imaging. Samples were imaged on a Zeiss
174 AxioImager.M2 with ApoTome. The TUNEL assay was performed with the ApopTag Red
175 *In Situ* Apoptosis Detection Kit (Millipore, S7165). Dissected larvae were fixed in 4%
176 paraformaldehyde, followed by a 10-minute wash in 75 μL equilibration buffer. Discs were
177 then submerged in 55 μL working strength TdT enzyme for 3 hours at 37°C. The reaction
178 was stopped by adding 1 mL stop/wash buffer and incubating for 10 minutes at room
179 temperature, followed by 3 washes in PBS. Primary staining was done by incubating 65
180 μL of the anti-digoxygenin rhodamine overnight at room temperature.
181

182 **Quantification and Statistical Analysis**

183 Adult wing measurements were gathered using the ImageJ software. GraphPad Prism
184 9.0 was used for statistical analysis and graphical representation. Graphs depict the mean

185 of each treatment, while error bars indicate the 95% confidence interval. For quantification
186 of DCP1 and PH3 positive cells, the cell counter plugin of ImageJ was used. For
187 quantification of *PCNA-GFP* signal, mean fluorescence intensity in pixels was measured
188 using ImageJ. To quantify Propidium Iodide (PI), due to the high variability of signal the
189 area of PI detection was calculated as a percent of the area of the *lexAop-GFP* reporter.
190 All experiments were repeated twice and the n for each experiment is indicated in the
191 figure legends. Statistical significance was evaluated in Prism using one-sample T-test or
192 One-Factor ANOVA, corrected for multiple comparisons by Tukey's or FDR.
193

194 **Data and Reagent Availability**

195 Strains and plasmids are available upon request, and details of stocks and reagents
196 used in this study are available in the Reagent Table. The authors affirm that all data
197 necessary for confirming the conclusions of the article are present within the article,
198 figures, and tables.

199 **Results**

200 **A genetic method to induce necrotic injury in the wing imaginal disc**

201 To study the response to necrosis we developed a method to induce damage in the larval
202 wing disc by adapting a system we previously established to study regeneration called
203 DUAL Control (Harris et al. 2020). This system utilizes a split version of the bacterial
204 *LexA*/*lexAOp* transcriptional regulator to transiently express a pro-apoptotic gene in the
205 distal wing tissue under the control of the *spalt* (*salm*) enhancer following a short heat
206 shock (Figure 1A). This apoptosis stimulates regeneration over the subsequent 24 to 48
207 hr, which can be quantitatively assessed by examining the degree to which the distal tip
208 of the wing is present in the adult fly (Harris et al. 2020). We previously used *lexAOp*-
209 driven *reaper* (*rpr*) to induce cell death (Harris et al. 2020), and have since established
210 another apoptosis-promoting transgene, *lexAOp-hep*^{CA}, a constitutive form of the JNK
211 kinase *hemipterous* (Adachi-Yamada et al. 1999). To study necrosis, we used the GluR1
212 protein, a murine glutamate receptor that regulates Ca^{2+} ion entry into a cell (Kohda et al.
213 2000). A characterized allele of this ion channel (*GluR1*^{LC}) confers constitutive activity,
214 leading to Ca^{2+} influx, osmotic swelling and catastrophic death of the cell (Kohda et al.
215 2000; Yang et al. 2013). We generated *lexAOp-GluR1*^{LC} and used it to build a version of
216 DUAL Control that expresses *GluR1*^{LC} in developing wing disc (Figure 1A and S1A-B).

217

218 To test our ability to induce damage using this system, we heat shocked larvae bearing
219 DUAL Control expressing *GluRI*^{LC} alongside discs ablated by *rpr* or *hep*^{CA} (hereafter
220 *DC*^{GluRI}, *DC*^{rpr} and *DC*^{hepCA}), using the pouch marker *nubbin* (*nub*) and the structural
221 marker *DE-cadherin* (*DE-cad*) to evaluate disc integrity (Figure 1C). Ablation with *DC*^{GluRI}

222 leads to a loss of tissue in the *salm* domain, shown by an absence of both markers (Figure
223 1D), which is similar to the loss of tissue resulting from ablation by DC^{rpr} (Figure 1E) and
224 DC^{hepCA} (Figure 1F). Ablation only occurs when all three transgenes that comprise the
225 DUAL Control system are present (Figure S1C-F). We next examined the degree to which
226 wing discs can regenerate following DC^{GluR1} ablation compared to DC^{rpr} and DC^{hepCA}.
227 Regeneration was assayed by appearance of the adult wing, scored for the presence of
228 the distal wing tip (Figure 1G and 1H) and measurement of the total wing area (Figure
229 1I). Ablation by DC^{rpr} and DC^{hepCA} in early L3 (84 hr after egg deposition, AED) leads to
230 significant regeneration, illustrated by both wing scoring and area (Figure 1H-I). Ablation
231 by DC^{GluRI} results in similar levels of ablation and regeneration (Figure 1H-I). The ability
232 of discs to regenerate is known to decline with developmental maturity from early to late
233 L3 (Harris et al. 2016; Harris et al. 2020). Ablation by each method in late L3 (108 hr AED)
234 results in a similar loss of distal wing tissue (Figure 1H-I). Together, these data show that
235 DC^{GluRI} can ablate the wing disc and induce regeneration at levels equivalent to that of
236 apoptosis-based methods.
237
238 To characterize how DC^{GluRI} induces damage we examined ablated discs for different cell
239 death markers. The loss of tissue in DC^{GluRI} coincides with strong propidium iodide (PI)
240 staining (Figure 2A, arrowhead, S2A and S2C), which labels cells with compromised
241 membranes such as those undergoing necrosis (Wlodkowic et al. 2011). Conversely, PI
242 staining of DC^{hepCA} ablated discs shows only weak PI (Figure 2B, S2B-C). As activated
243 caspases are a hallmark of apoptosis but not necrosis, we also stained ablated discs for
244 the cleaved caspase DCP1. As expected, ablation with DC^{rpr} or DC^{hepCA} yields a strong

245 DCP1 signal concentrated within the *salm* domain (Figures 2E-F). Sporadic caspase-
246 positive cells are seen outside of the ablation domain in all discs, likely due to the heat
247 shock used to activate ablation (Figure 2C). Surprisingly, discs ablated with DC^{GluRI} also
248 have significant levels of DCP1 (Figure 2D). However, most of this staining is observed
249 in the lateral wing pouch at a distance from the ablated tissue (Figure 2D, arrowheads).
250 These DCP1 positive cells are clearly separable from the dying cells in the *salm* domain.
251 They are also not a result of dying cells moving away from the site of injury, as a *lexAop-*
252 *GFP* transgene that labels ablated cells fails to mark the caspase positive cells outside of
253 the *salm* domain (Figures 2G and 2H, arrowheads, S2D, S2F). This contrasts with
254 DC^{hepCA} discs where GFP and DCP1 almost entirely overlap (Figure 2I and 2J, S2E), with
255 very few DCP1-positive cells observed outside of the *salm* domain (Figure S2F). Thus,
256 the observed apoptosis does not occur in cells killed by *GluRI* but is instead induced in
257 neighboring cells.
258
259 In addition to promoting apoptosis, caspases can perform other cellular functions in
260 imaginal discs unrelated to cell death (Su 2020). To examine whether the detected
261 caspase activity is related to cell death we also performed a TUNEL assay, which reveals
262 strong staining in the caspase positive cells found outside of the *salm* domain in DC^{GluRI}
263 discs (Figure 2K, arrowheads). This is consistent with *GluRI*-induced caspase activity
264 leading to cell death, as in DC^{rpr} ablated discs (Figure 2L). We also observed a separate
265 weaker TUNEL signal in DC^{GluRI} ablated discs within the *salm* domain, indicative of DNA
266 fragmentation (Figure 2K, open arrowhead), which has previously been described in
267 necrotic cells (Grasl-Kraupp et al. 1995). Together, these results demonstrate that

268 ablation with *DC*^{GluR1} leads to tissue loss and stimulates regeneration, but also
269 unexpectedly activates widespread apoptosis in the surrounding cells at a distance from
270 the injury.
271
272 **Tissue loss via *DC*^{GluRI} ablation occurs independent of caspase activity**
273 To understand if the non-autonomous apoptosis observed in *DC*^{GluRI} discs contributes to
274 tissue loss, or alternatively is a consequence of it, we used the baculoviral caspase
275 inhibitor P35 to block apoptosis in the entire pouch (Hay et al. 1994). DUAL Control
276 permits the expression of *UAS*-driven transgenes in the wing pouch independent of
277 ablation under the control of a flip-out GAL4 (*DVE>>GAL4*), which is initiated by the same
278 heat shock that triggers ablation and persists throughout the subsequent regeneration
279 period (Figure 1B and S1A-B (Harris et al. 2020)). To test P35 in the DUAL Control
280 system, we first blocked apoptosis in *rpr* ablated discs using *UAS-p35* (*DC*^{rpr}*>>p35*).
281 These discs have an intact pouch epithelium, shown by Nub and DE-cad staining (Figure
282 3A), and lack TUNEL staining (Figure S3A). DCP1 is still detected in *DC*^{rpr}*>>p35* discs
283 although the intense punctate staining is replaced by a diffuse cytoplasmic signal (Figures
284 3C and 3D), which has been reported previously when caspase activity is inhibited by
285 P35 (Perez-Garijo et al. 2013). Conversely, P35 is unable to prevent tissue loss resulting
286 from *DC*^{GluRI} ablation, indicated by the absence of Nub and DE-cad in the pouch (Figure
287 3B) and presence PI staining in the *salm* domain (Figure 3G). The appearance of the
288 DCP1 staining in *DC*^{GluRI}*>>p35* discs is also diffuse (Figures 3E and 3F) like that of
289 *DC*^{rpr}*>>p35*, while TUNEL staining in the lateral pouch is now absent (Figure 3H),
290 indicating that the apoptosis in these regions is being blocked. However, the weak TUNEL

291 signal within the cells of the *salm* domain is still observed (Figure 3H, open arrowhead).
292 These data suggest that inhibition of caspase activity cannot block tissue loss caused by
293 DC^{GluR1} ablation.
294
295 In agreement with the observed disc phenotypes, blocking apoptosis with P35 in *rpr*
296 ablated discs results in full sized adult wings, shown by scoring and wing area
297 measurements of both early and late L3 ablated organisms (Figures 3I, 3K-K' and 3M).
298 By contrast, blocking apoptosis in DC^{GluRI} ablated discs does not prevent tissue loss, as
299 adult wings that develop from DC^{GluRI}>>*p35* discs have similar phenotypes to discs
300 ablated in the absence of P35 (Figures 3J, 3L-L' and 3M). Together these observations
301 suggest that DC^{GluR1} can kill cells independent of caspase activity, and that the apoptotic
302 cells seen at a distance from the wound are a consequence of this tissue loss rather than
303 being required for it. Thus, we refer to DC^{GluRI}-induced tissue loss as necrotic ablation,
304 and the non-autonomous caspase-positive cell death in the surrounding tissue as
305 necrosis-induced apoptosis (NiA).
306
307 In our adult wing assays we noted a distinct category of wings from DC^{GluRI}>>*p35* animals
308 that are poorly patterned and have increased blistering and folding (Figure S3B and S3C).
309 This phenotype also occurs in DC^{hepCA}>>*p35* discs (Figure S3C). Blocking caspase
310 activity with P35 in cells undergoing apoptosis can produce undead cells that continue to
311 express mitogenic genes like *wg* and *dpp* downstream of JNK signaling, leading to
312 tumorous overgrowth of the surrounding tissue (Martin et al. 2009; Perez-Garijo et al.
313 2004; Ryoo et al. 2004). Indeed, DC^{hepCA}>>*p35* have significant ectopic *wg* expression in

314 the ablation domain overlapping the diffuse DCP1 compared to ablation in the absence
315 of P35 (Figure S3D and S3E). We hypothesized that blocking apoptosis in *DC^{GluRI}>>p35*
316 ablated discs might result in undead cells that produce the overgrown adult wing
317 phenotype. However, in *DC^{GluRI}>>p35* discs ectopic *wg* is only detected near to the wound
318 edge, and not in the surrounding pouch where undead NiA would be expected to produce
319 ectopic *wg* (Figure S3F), and *Dpp* expression shown by a *Dpp-lacZ* reporter is not altered
320 (data not shown). To test whether the observed *wg* is important for overgrowth we
321 knocked it down in the entire pouch (*DC^{GluRI}>>p35, wg^{RNAi}),* which eliminated the
322 overgrowth phenotype (Fig S3G-I). Since ectopic *wg* is only associated with apoptotic
323 cells at the wound edge it is possible that it is only these cells that contribute to overgrowth
324 when forced to become undead. To test this, we used a *DR^{WNT}-GAL80* transgene in
325 *DC^{GluRI}>>p35* discs to limit p35 expression to the regions of the pouch where NiA cells
326 occur (Figure S3J-L). In this experiment the overgrowth phenotype is significantly reduced
327 (Figure S3C), demonstrating that NiA do not strongly contribute to overgrowth after
328 becoming undead. Alongside the observation that they do not express *wg*, these data
329 suggest that undead NiA cells do not activate the same genetic pathways as undead cells
330 generated by directly activating apoptosis in the presence of P35.
331

332 **NiA and wound edge apoptosis originate separately**

333 To investigate the origin and timing of the NiA seen in *DC^{GluRI}* discs we performed a time
334 course of ablation and regeneration (Figure 4). To observe the formation of regenerating
335 cells we took advantage of the *DR^{WNT}* transgene, a damage-specific fluorescent reporter
336 of WNT expression, which is activated upon ablation and represents one of the earliest

337 signaling events in disc regeneration (Figure 4A-4F)(Harris et al. 2016). *DR*^{WNT}
338 expression becomes apparent at the wound edge 6 hr post-ablation with *DC*^{GluR1} (Figure
339 4B), while most apoptotic cells in this region become obvious at around 12 hr (Figure 4C,
340 arrowhead). NiA populations are still not observed at this timepoint and only occur at 18
341 hr post ablation after the appearance of wound edge apoptosis and *DR*^{WNT} activity (Figure
342 4D, arrowheads). The NiA persists as regeneration proceeds (Figure 4E), and by 48 hr,
343 when *DR*^{WNT} expression is diminished, the DCP1-positive cellular debris appears to be
344 pushed dorsally and ventrally possibly as a result of pouch growth (Figure 4F). At this
345 time point the pouch is fully restored, indicated by *nub* expression (Figure 4G).
346 Interestingly, *DR*^{WNT} activity is never observed beyond the wound edge and does not
347 occur in NiA cells. Thus, the time course shows that formation of NiA is not only spatially
348 distinct from the wound edge apoptosis and damage associated signaling shown by
349 *DR*^{WNT}, but is also temporally separated from it. These observations suggest that these
350 two populations might arise via different mechanisms.
351

352 **NiA is independent of JNK signaling**

353 The *DR*^{WNT} reporter used in the time course is directly activated by JNK signaling (Harris
354 et al. 2016). Since *DR*^{WNT} expression is restricted to the wound edge, and JNK signaling
355 is a key pathway that regulates both apoptosis and proliferation in response to damage
356 (Pinal et al. 2019), we evaluated JNK signaling in *DC*^{GluRI} ablated discs. Using a reporter
357 for AP-1 activity (*AP-1-GFP* (Chatterjee and Bohmann 2012)) we found that JNK signaling
358 is present only in wound edge cells and not in cells undergoing NiA (Figure 5A), consistent
359 with the *DR*^{WNT} reporter expression. Examination of the JNK target genes *puc, wg* and

360 *Mmp1* supports these results (Figures 5B, 5C and 5D), suggesting that necrotic ablation
361 leads to JNK upregulation and low levels of apoptosis at the wound edge, and induces
362 NiA at a distance without activating JNK.
363
364 To test whether NiA does indeed occur independent of JNK, we investigated how altering
365 different elements of the JNK pathway might influence either the wound edge or NiA
366 populations in DC^{GluRI} ablated discs. Knockdown of the JNK kinase *hep* using RNAi
367 reduces the expression of the JNK target *Mmp1* but does not strongly alter apoptosis at
368 the wound edge (Figure 5E). Importantly, NiA cells are still observed in the absence of
369 *hep* (Figure 5E). This result is confirmed using a *hep* hemizygous mutant (hep^{r75}/Y),
370 although the level of apoptosis across the whole disc is somewhat reduced when using
371 this allele (Figure S4A). The expression of a dominant negative form of the JNK *basket*
372 ($UAS\text{-}bsk^{DN}$) strongly suppresses *Mmp1* expression (Figure 5F), and unlike the loss of
373 *hep*, bsk^{DN} also reduces apoptosis at the wound edge (Figure 5F), suggesting that this
374 cell death is dependent on *bsk*. The population of NiA cells is also unaffected in this
375 background (Figure 5F), supporting the idea that NiA formation does not depend on JNK
376 signaling. RNAi knockdown of *bsk* also confirms these results (Figure S4B). Since the
377 loss of *bsk*, but not *hep*, seems to influence wound edge apoptosis, we also targeted an
378 alternative JNK kinase, *Mkk4*, for knockdown in DC^{GluRI} ablated discs. Unlike *hep*,
379 reduction of *Mkk4* levels reduces both the apoptosis and *Mmp1* expression at the wound
380 edge, but again has no influence on the appearance of NiA (Figure 5G). We also reduced
381 expression of a TNF receptor *grindelwald* (*grnd*) and TNF ligand *egr* using RNAi. Neither
382 manipulation affected the apoptosis or JNK activity at the wound edge or the appearance

383 of the cells undergoing NiA outside the ablated domain (Figure S4C and S4D). Moreover,
384 a reporter for *egr* expression (*egr-GAL4 ; UAS-GFP*) shows no upregulation of *egr* at the
385 wound edge or in cells undergoing NiA (Figure S4H-S4J). Interestingly however, *egr*
386 expression that is normally observed in adult muscle precursor cells under the notum is
387 reduced upon ablation (Figure S4H-S4J). Overall, these data suggest that necrotic
388 ablation induces low levels of apoptosis and JNK signaling at the wound edge, which
389 occurs downstream of a JNK receptor *grnd* but is dependent on both *Mkk4* and *bsk*, while
390 also generating NiA at a distance via a JNK-independent signal.
391
392 As NiA does not appear to require JNK, we sought to investigate factors upstream of the
393 observed activated caspase DCP1 that might be required to produce NiA following
394 necrotic ablation. We used an RNAi targeting the dIAP1 inhibitor *rpr*, which activates cell
395 death immediately upstream of initiator caspases. Knockdown of *rpr* leads to a moderate
396 reduction in apoptosis at the wound edge, but also reduces NiA formation (Figure S4E).
397 Mutation of another dIAP1 inhibitor, *head involution defective* (*hid*), did not have an effect
398 (Figure S4F). However, when a miRNA targeting *rpr*, *hid* and another dIAP1 inhibitor *grim*
399 was used (*UAS-miRHG*), NiA formation was eliminated (Figure 5H), as was the cell death
400 normally observed at the wound edge, indicating that more than one of these genes are
401 required for both wound edge apoptosis and NiA. Importantly, DC^{GluRI}-induced tissue loss
402 still clearly occurs even in the absence of NiA (Figure S4G), while JNK signaling indicated
403 by *Mmp1* expression is observed, albeit at a reduced level (Figure 5H). JNK signaling is
404 thought to activate a feedforward mechanism through DRONC, reactive oxygen species
405 (ROS) and hemocytes (Amcheslavsky et al. 2018), and therefore this diminished Mmp1

406 labeling could be due to interference with this mechanism. Overall, these results suggest
407 that necrotic ablation leads to apoptosis at the wound edge and NiA in the surrounding
408 pouch, and although each is regulated by different activating signals, they rely on the
409 same downstream effectors, *rpr, hid,* and *grim*, to kill cells.
410

411 **NiA is required for damage-induced proliferation and subsequent regeneration**

412 To understand the potential contribution of NiA to regeneration we examined how the
413 appearance of NiA coincides with regenerative proliferation following necrotic ablation.
414 We used reporters for *E2F* (*PCNA-GFP*) and *Cyclin E* (*cycE-GFP*), and PH3 staining to
415 examine changes in proliferation that occur during regeneration. These markers show
416 that proliferation induced by necrotic ablation does not significantly increase in the wing
417 pouch until around 24 hr, after the formation of NiA at 18 hr (Figure 6A-B, S5A-E). To test
418 whether NiA regulates this localized proliferation, we sought to eliminate this apoptosis
419 following DC^{GluRI} ablation. As NiA is unaffected by blocking JNK signaling, and P35 allows
420 dying cells to persist in the disc which could complicate our analysis due to the observed
421 overgrowth (Figure S3), we used *UAS-miRHG* to prevent the formation of NiA. The lack
422 of NiA in the pouch following necrotic ablation results in a loss of *PCNA-GFP* upregulation
423 that is normally seen at 24 hr (Figure 6C), as well as diminished PH3 levels (Figure S5E),
424 suggesting that NiA is required for regenerative proliferation. Importantly, JNK signaling
425 at the wound edge is still observed following *miRHG* expression, indicated by the
426 presence of *Mmp1* (Figure 6C), demonstrating that proliferation following necrotic ablation
427 is not dependent solely on JNK activity from the wound, but also requires NiA.
428

429 We next examined how blocking NiA might influence the discs capacity to regenerate.
430 Evaluating adult wings that develop from *DC*^{GluRI}*>>miRHG* discs shows they have a
431 reduced ability to regenerate compared to control discs (Figure 6F-G). This result is
432 significant, as blocking apoptosis with *miRHG* would normally be expected to improve
433 regeneration, as it does in *DC*^{rpr} ablated discs (Figure 6E). However, in this experiment
434 apoptosis is blocked throughout the pouch and is not specific to the NiA. Therefore, we
435 used *DR*^{WNT}*-GAL80* to limit *miRHG* expression solely to the surrounding pouch where
436 NiA develops and allow wound edge apoptosis to still occur (Figure 6D). When wound
437 edge apoptosis can still occur but NiA is blocked, regeneration is still strongly inhibited in
438 both early and late L3 discs (Figure 6F-G), demonstrating that NiA is specifically required
439 for regeneration in response to necrosis.
440

441 **Discussion**

442 **Necrosis induces apoptosis at a distance in the wing imaginal disc**

443 Necrotic ablation induces apoptosis in cells in two regions of the injured disc: at the wound
444 edge and more extensively in the surrounding pouch. These two populations of dying
445 cells are likely induced by separate activating signals, rely on the same downstream
446 effectors, and contribute differently to regeneration (Figure 7). The wound edge apoptosis
447 coincides with JNK activity and is likely dependent on it, as interference with *bsk* strongly
448 limits the caspase observed at the wound. The factors that can activate JNK signaling,
449 and those downstream that regulate whether cells subsequently proliferate or undergo
450 apoptosis, are complex and context dependent (La Marca and Richardson 2020; Pinal et
451 al. 2019). However, our experiments show that pathway activation following necrotic

452 ablation does not rely on a receptor for JNK, *grnd*, and requires the JNK kinase *Mkk4*
453 more than *hep*. There are a number of signals that can induce JNK activity in this way,
454 including loss of polarity, mechanical inputs and the release of immediate stress signals
455 such as ROS (La Marca and Richardson 2020). ROS has been shown to upregulate both
456 JNK and P38, another factor that regulates proliferation and apoptosis, via Ask1/AKT
457 (Santabarbara-Ruiz et al. 2019; Santabarbara-Ruiz et al. 2015), while ROS is known to
458 be an important regulator of regeneration in the wing disc (Brock et al. 2017; Khan et al.
459 2017; Santabarbara-Ruiz et al. 2019; Santabarbara-Ruiz et al. 2015). Thus, it is possible
460 that JNK signaling and the associated apoptosis at the wound edge induced by necrotic
461 ablation is mediated via this pathway. It is likely that this JNK activity contributes to
462 recovery following necrosis, as it does in apoptosis-induced regeneration. However, our
463 observation that blocking NiA limits regeneration, despite wound edge apoptosis and JNK
464 being unaffected, suggests that regeneration does not solely depend on JNK signaling.
465
466 The signals that lead to the NiA at a distance from the necrotic injury are less clear,
467 however. A related phenomenon to the one we have observed, in which cells undergoing
468 programmed cell death induce additional non-autonomous apoptosis, has been
469 described in the wing imaginal disc and the mouse hair follicle (Perez-Garijo et al. 2013).
470 However, in both contexts these events are induced by apoptotic cell death rather than
471 necrosis, and are mediated by JNK signaling, unlike NiA. In a parallel observation to that
472 of apoptotic cells communicating with surrounding tissues, studies have shown that cells
473 undergoing necrosis might also release factors that regulate the behavior of neighboring
474 cells. These factors are collectively known as damage associated molecular patterns or

475 DAMPs (Gong et al. 2020; Roh and Sohn 2018). Such signals often consist of
476 endogenous intracellular molecules like cytoskeletal components, DNA, RNA, histones
477 and metabolites, which are passively released and inappropriately exposed to the
478 extracellular environment. DAMPs are detected by immune cells that in turn activate
479 immune pathways to mount a stress response known as sterile inflammation (Gong et al.
480 2020). Beyond these initial inflammatory responses, DAMPs are also important for
481 orchestrating the subsequent steps in tissue repair and regeneration (Venereau et al.
482 2015). In *Drosophila*, the actin-binding protein α-actinin has been shown to act as a
483 DAMP when purified and injected into adult flies, inducing a humoral immune response
484 in the form of cytokine signal activation specifically in the fat body (Gordon et al. 2018;
485 Srinivasan et al. 2016). Similarly, apoptotic-deficient *Drosophila* constitutively activate
486 immune signaling in the larval fat body due to the presence of circulating DAMPs in the
487 hemolymph (Ming et al. 2014). Recently it was shown that imaginal disc damage leads to
488 the upregulation of circulating metabolites produced by the fat body, which are necessary
489 for proper disc repair (Kashio and Miura 2020), highlighting the importance of interorgan
490 communication in the context of regeneration. Thus, one possibility is that necrotic cells
491 release DAMP signals to induce pro-regenerative NiA in the disc via an immune response
492 involving the fat body. The role of hemocytes, an essential population of immune cells, in
493 the regeneration of damaged imaginal discs has also been explored following physical
494 and apoptotic damage (Fogarty et al. 2016; Katsuyama and Paro 2013; Pastor-Pareja et
495 al. 2008), and in the context of sterile inflammation that occurs following necrosis
496 (Shaukat et al. 2015). Considering the vital roles hemocytes play in these processes it is
497 possible they also mediate immune or other signals to induce NiA formation. Alternatively,

498 DAMPs are also known to have stimulatory effects on non-immune cells (Chen and
499 Nunez 2010; Gong et al. 2020), and thus could be sensed directly by the immediately
500 surrounding pouch tissues to induce NiA. Going forward it will be important to ascertain
501 both the identity of the signal and the physiological mechanism by which necrosis leads
502 to non-autonomous cell death in the wing disc.
503

504 **NiA is necessary for proliferation and subsequent regeneration**

505 Our data show that blocking NiA following necrosis inhibits the localized proliferation that
506 promotes tissue repair, strongly suggesting that NiA is a vital part of the recovery process.
507 How this type of cell death might promote proliferation is still unclear, however. Apoptosis-
508 induced proliferation (AiP) is a well-established phenomenon, in which dying cells release
509 mitogens, such as *wg* and *dpp*, downstream of JNK signaling to stimulate localized
510 proliferation (Fogarty and Bergmann 2017; Perez-Garijo and Steller 2015). These
511 mitogens act via a feed forward mechanism that involves the release of ROS, recruitment
512 of hemocytes and induction of further JNK signaling to promote repair (Amcheslavsky et
513 al. 2018; Fogarty and Bergmann 2017; Fogarty et al. 2016). By contrast, we have shown
514 that cells undergoing NiA do not detectably express *wg* or *dpp*, even in an undead state,
515 and do not activate JNK signaling. Although we have not ruled out other characterized
516 mitogens being involved, these findings suggest that NiA may not promote proliferation
517 via the established AiP mechanism. An important consideration is whether cells
518 undergoing NiA release specific signals to direct tissue regrowth, as seen with AiP, or if
519 the tissue loss resulting from necrosis and NiA is instead sensed more generally at the
520 level of the whole disc, stimulating coordinated regrowth in addition to localized

521 proliferation (Hariharan 2015). The identification of signals produced by NiA cells and a
522 better understanding of proliferation rates across a recovering disc will help to reveal the
523 contribution of these different mechanisms to necrosis-induced regeneration.
524
525 Tissue necrosis is associated with many types of traumatic injury and diseases in
526 humans, including ischemic injuries, infections and cancer. Using model systems, like the
527 one we have developed here, to understand how necrotic cells impact neighboring
528 healthy tissues, and how these tissues enact mechanisms to effectively recover, may help
529 to identify therapeutic interventions that promote healing in tissues which otherwise
530 struggle to recover from necrosis, such as those of humans.

531 **References**

532 Adachi-Yamada T, Fujimura-Kamada K, Nishida Y, Matsumoto K. 1999. Distortion of
533 proximodistal information causes jnk-dependent apoptosis in drosophila wing.
534 Nature. 400(6740):166-169.
535 Amcheslavsky A, Wang S, Fogarty CE, Lindblad JL, Fan Y, Bergmann A. 2018. Plasma
536 membrane localization of apoptotic caspases for non-apoptotic functions.
537 Developmental cell. 45(4):450-464 e453.
538 Beira JV, Paro R. 2016. The legacy of drosophila imaginal discs. Chromosoma.
539 125(4):573-592.
540 Bergmann A, Steller H. 2010. Apoptosis, stem cells, and tissue regeneration. Sci Signal.
541 3(145):re8.
542 Bianchi ME. 2007. Damps, pamps and alarmins: All we need to know about danger. J
543 Leukoc Biol. 81(1):1-5.
544 Bilak A, Uyetake L, Su TT. 2014. Dying cells protect survivors from radiation-induced cell
545 death in drosophila. PLoS Genet. 10(3):e1004220.
546 Bonne SL, Kadri SS. 2017. Evaluation and management of necrotizing soft tissue
547 infections. Infect Dis Clin North Am. 31(3):497-511.
548 Brock AR, Seto M, Smith-Bolton RK. 2017. Cap-n-collar promotes tissue regeneration by
549 regulating ros and jnk signaling in the drosophila melanogaster wing imaginal disc.
550 Genetics. 206(3):1505-1520.
551 Chatterjee N, Bohmann D. 2012. A versatile phic31 based reporter system for measuring
552 ap-1 and nrf2 signaling in drosophila and in tissue culture. PLoS One. 7(4):e34063.
553 Chen GY, Nunez G. 2010. Sterile inflammation: Sensing and reacting to damage. Nat
554 Rev Immunol. 10(12):826-837.
555 Chera S, Ghila L, Dobretz K, Wenger Y, Bauer C, Buzgariu W, Martinou JC, Galliot B.
556 2009. Apoptotic cells provide an unexpected source of wnt3 signaling to drive
557 hydra head regeneration. Developmental cell. 17(2):279-289.
558 Everetts NJ, Worley MI, Yasutomi R, Yosef N, Hariharan IK. 2021. Single-cell
559 transcriptomics of the drosophila wing disc reveals instructive epithelium-to-
560 myoblast interactions. Elife. 10.

561 Fogarty CE, Bergmann A. 2015. The sound of silence: Signaling by apoptotic cells. Curr
562 Top Dev Biol. 114:241-265.
563 Fogarty CE, Bergmann A. 2017. Killers creating new life: Caspases drive apoptosis-
564 induced proliferation in tissue repair and disease. Cell Death Differ. 24(8):1390-
565 1400.
566 Fogarty CE, Diwanji N, Lindblad JL, Tare M, Amcheslavsky A, Makhijani K, Bruckner K,
567 Fan Y, Bergmann A. 2016. Extracellular reactive oxygen species drive apoptosis-
568 induced proliferation via drosophila macrophages. Curr Biol. 26(5):575-584.
569 Fox DT, Cohen E, Smith-Bolton R. 2020. Model systems for regeneration: Drosophila.
570 Development. 147(7).
571 Fuchs Y, Steller H. 2011. Programmed cell death in animal development and disease.
572 Cell. 147(4):742-758.
573 Fuchs Y, Steller H. 2015. Live to die another way: Modes of programmed cell death and
574 the signals emanating from dying cells. Nat Rev Mol Cell Biol. 16(6):329-344.
575 Gong T, Liu L, Jiang W, Zhou R. 2020. Damp-sensing receptors in sterile inflammation
576 and inflammatory diseases. Nat Rev Immunol. 20(2):95-112.
577 Gordon O, Henry CM, Srinivasan N, Ahrens S, Franz A, Deddouche S, Chakravarty P,
578 Phillips D, George R, Kjaer S et al. 2018. Alpha-actinin accounts for the bioactivity
579 of actin preparations in inducing stat target genes in drosophila melanogaster.
580 Elife. 7.
581 Grasl-Kraupp B, Ruttkay-Nedecky B, Koudelka H, Bukowska K, Bursch W, Schulte-
582 Hermann R. 1995. In situ detection of fragmented DNA (tunel assay) fails to
583 discriminate among apoptosis, necrosis, and autolytic cell death: A cautionary
584 note. Hepatology. 21(5):1465-1468.
585 Hacker G. 2018. Apoptosis in infection. Microbes Infect. 20(9-10):552-559.
586 Hakkarainen TW, Kopari NM, Pham TN, Evans HL. 2014. Necrotizing soft tissue
587 infections: Review and current concepts in treatment, systems of care, and
588 outcomes. Curr Probl Surg. 51(8):344-362.
589 Hariharan IK. 2015. Organ size control: Lessons from drosophila. Developmental cell.
590 34(3):255-265.

591 Hariharan IK, Serras F. 2017. Imaginal disc regeneration takes flight. Curr Opin Cell Biol.
592 48:10-16.
593 Harris RE, Setiawan L, Saul J, Hariharan IK. 2016. Localized epigenetic silencing of a
594 damage-activated wnt enhancer limits regeneration in mature drosophila imaginal
595 discs. Elife. 5.
596 Harris RE, Stinchfield MJ, Nystrom SL, McKay DJ, Hariharan IK. 2020. Damage-
597 responsive, maturity-silenced enhancers regulate multiple genes that direct
598 regeneration in drosophila. Elife. 9.
599 Hay BA, Wolff T, Rubin GM. 1994. Expression of baculovirus p35 prevents cell death in
600 drosophila. Development. 120(8):2121-2129.
601 Huh JR, Guo M, Hay BA. 2004. Compensatory proliferation induced by cell death in the
602 drosophila wing disc requires activity of the apical cell death caspase dronc in a
603 nonapoptotic role. Curr Biol. 14(14):1262-1266.
604 Kashio S, Miura M. 2020. Kynurenine metabolism in the fat body non-autonomously
605 regulates imaginal disc repair in drosophila. iScience. 23(12):101738.
606 Katsuyama T, Paro R. 2013. Innate immune cells are dispensable for regenerative growth
607 of imaginal discs. Mech Dev. 130(2-3):112-121.
608 Khan SJ, Abidi SNF, Skinner A, Tian Y, Smith-Bolton RK. 2017. The drosophila duox
609 maturation factor is a key component of a positive feedback loop that sustains
610 regeneration signaling. PLoS Genet. 13(7):e1006937.
611 Kohda K, Wang Y, Yuzaki M. 2000. Mutation of a glutamate receptor motif reveals its role
612 in gating and delta2 receptor channel properties. Nat Neurosci. 3(4):315-322.
613 Konstantinidis K, Whelan RS, Kitsis RN. 2012. Mechanisms of cell death in heart disease.
614 Arterioscler Thromb Vasc Biol. 32(7):1552-1562.
615 La Marca JE, Richardson HE. 2020. Two-faced: Roles of jnk signalling during
616 tumourigenesis in the drosophila model. Front Cell Dev Biol. 8:42.
617 Li F, Huang Q, Chen J, Peng Y, Roop DR, Bedford JS, Li CY. 2010. Apoptotic cells
618 activate the "phoenix rising" pathway to promote wound healing and tissue
619 regeneration. Sci Signal. 3(110):ra13.

620 Liu K, Ding L, Li Y, Yang H, Zhao C, Lei Y, Han S, Tao W, Miao D, Steller H et al. 2014.
621 Neuronal necrosis is regulated by a conserved chromatin-modifying cascade. Proc
622 Natl Acad Sci U S A. 111(38):13960-13965.
623 Martin FA, Perez-Garijo A, Morata G. 2009. Apoptosis in drosophila: Compensatory
624 proliferation and undead cells. Int J Dev Biol. 53(8-10):1341-1347.
625 Masi L, Falchetti A, Brandi ML. 2007. Osteonecrosis in genetic disorders. Clin Cases
626 Miner Bone Metab. 4(1):27-29.
627 Milner PF, Kraus AP, Sebes JI, Sleeper LA, Dukes KA, Embury SH, Bellevue R, Koshy
628 M, Moohr JW, Smith J. 1991. Sickle cell disease as a cause of osteonecrosis of
629 the femoral head. N Engl J Med. 325(21):1476-1481.
630 Ming M, Obata F, Kuranaga E, Miura M. 2014. Persephone/spatzle pathogen sensors
631 mediate the activation of toll receptor signaling in response to endogenous danger
632 signals in apoptosis-deficient drosophila. J Biol Chem. 289(11):7558-7568.
633 Pastor-Pareja JC, Wu M, Xu T. 2008. An innate immune response of blood cells to tumors
634 and tissue damage in drosophila. Dis Model Mech. 1(2-3):144-154; discussion
635 153.
636 Patel S. 2018. Danger-associated molecular patterns (damps): The derivatives and
637 triggers of inflammation. Curr Allergy Asthma Rep. 18(11):63.
638 Pellettieri J, Fitzgerald P, Watanabe S, Mancuso J, Green DR, Sanchez Alvarado A.
639 2010. Cell death and tissue remodeling in planarian regeneration. Dev Biol.
640 338(1):76-85.
641 Perez-Garijo A, Fuchs Y, Steller H. 2013. Apoptotic cells can induce non-autonomous
642 apoptosis through the tnf pathway. Elife. 2:e01004.
643 Perez-Garijo A, Martin FA, Morata G. 2004. Caspase inhibition during apoptosis causes
644 abnormal signalling and developmental aberrations in drosophila. Development.
645 131(22):5591-5598.
646 Perez-Garijo A, Steller H. 2015. Spreading the word: Non-autonomous effects of
647 apoptosis during development, regeneration and disease. Development.
648 142(19):3253-3262.

649 Pinal N, Calleja M, Morata G. 2019. Pro-apoptotic and pro-proliferation functions of the
650 jnk pathway of drosophila: Roles in cell competition, tumorigenesis and
651 regeneration. Open Biol. 9(3):180256.
652 Radak D, Katsiki N, Resanovic I, Jovanovic A, Sudar-Milovanovic E, Zafirovic S, Mousad
653 SA, Isenovic ER. 2017. Apoptosis and acute brain ischemia in ischemic stroke.
654 Curr Vasc Pharmacol. 15(2):115-122.
655 Roh JS, Sohn DH. 2018. Damage-associated molecular patterns in inflammatory
656 diseases. Immune Netw. 18(4):e27.
657 Ryoo HD, Gorenc T, Steller H. 2004. Apoptotic cells can induce compensatory cell
658 proliferation through the jnk and the wingless signaling pathways. Developmental
659 cell. 7(4):491-501.
660 Santabarbara-Ruiz P, Esteban-Collado J, Perez L, Viola G, Abril JF, Milan M, Corominas
661 M, Serras F. 2019. Ask1 and akt act synergistically to promote ros-dependent
662 regeneration in drosophila. PLoS Genet. 15(1):e1007926.
663 Santabarbara-Ruiz P, Lopez-Santillan M, Martinez-Rodriguez I, Binagui-Casas A, Perez
664 L, Milan M, Corominas M, Serras F. 2015. Ros-induced jnk and p38 signaling is
665 required for unpaired cytokine activation during drosophila regeneration. PLoS
666 Genet. 11(10):e1005595.
667 Shaukat Z, Liu D, Gregory S. 2015. Sterile inflammation in drosophila. Mediators Inflamm.
668 2015:369286.
669 Srinivasan N, Gordon O, Ahrens S, Franz A, Deddouche S, Chakravarty P, Phillips D,
670 Yunus AA, Rosen MK, Valente RS et al. 2016. Actin is an evolutionarily-conserved
671 damage-associated molecular pattern that signals tissue injury in drosophila
672 melanogaster. Elife. 5.
673 Su TT. 2015. Non-autonomous consequences of cell death and other perks of being
674 metazoan. AIMS Genet. 2(1):54-69.
675 Su TT. 2020. Non-apoptotic roles of apoptotic proteases: New tricks for an old dog. Open
676 Biol. 10(8):200130.
677 Suzanne M, Steller H. 2013. Shaping organisms with apoptosis. Cell Death Differ.
678 20(5):669-675.

679 Tseng AS, Adams DS, Qiu D, Koustubhan P, Levin M. 2007. Apoptosis is required during
680 early stages of tail regeneration in xenopus laevis. Dev Biol. 301(1):62-69.
681 Venereau E, Ceriotti C, Bianchi ME. 2015. Damps from cell death to new life. Front
682 Immunol. 6:422.
683 Vriz S, Reiter S, Galliot B. 2014. Cell death: A program to regenerate. Curr Top Dev Biol.
684 108:121-151.
685 Wlodkowic D, Telford W, Skommer J, Darzynkiewicz Z. 2011. Apoptosis and beyond:
686 Cytometry in studies of programmed cell death. Methods Cell Biol. 103:55-98.
687 Wong RS. 2011. Apoptosis in cancer: From pathogenesis to treatment. J Exp Clin Cancer
688 Res. 30:87.
689 Worley MI, Setiawan L, Hariharan IK. 2012. Regeneration and transdetermination in
690 drosophila imaginal discs. Annu Rev Genet. 46:289-310.
691 Yang Y, Hou L, Li Y, Ni J, Liu L. 2013. Neuronal necrosis and spreading death in a
692 drosophila genetic model. Cell Death Dis. 4:e723.
693 Yuan J. 2009. Neuroprotective strategies targeting apoptotic and necrotic cell death for
694 stroke. Apoptosis. 14(4):469-477.
695

696 **Acknowledgements**

697 The authors would like to thank Dr. David Bilder and Dr. Iswar Hariharan of UC Berkeley
698 and Dr. Tian Xie of the Stowers Institute for their gift of stocks. We thank Ayla Zustra and
699 current members of the Harris lab for useful feedback. We thank the Bloomington Stock
700 Center, Developmental Studies Hybridoma Bank, and BestGene for stocks, reagents, and
701 services.

702

703 **Funding Information**

The funders had no role in study design, data collection and interpretation, or the decision to submit the work for publication. This work was supported by a grant from the NICHD 1 R21 HD102765-01 to Robin Harris.

Competing interests

No competing interests declared.

Figure 1

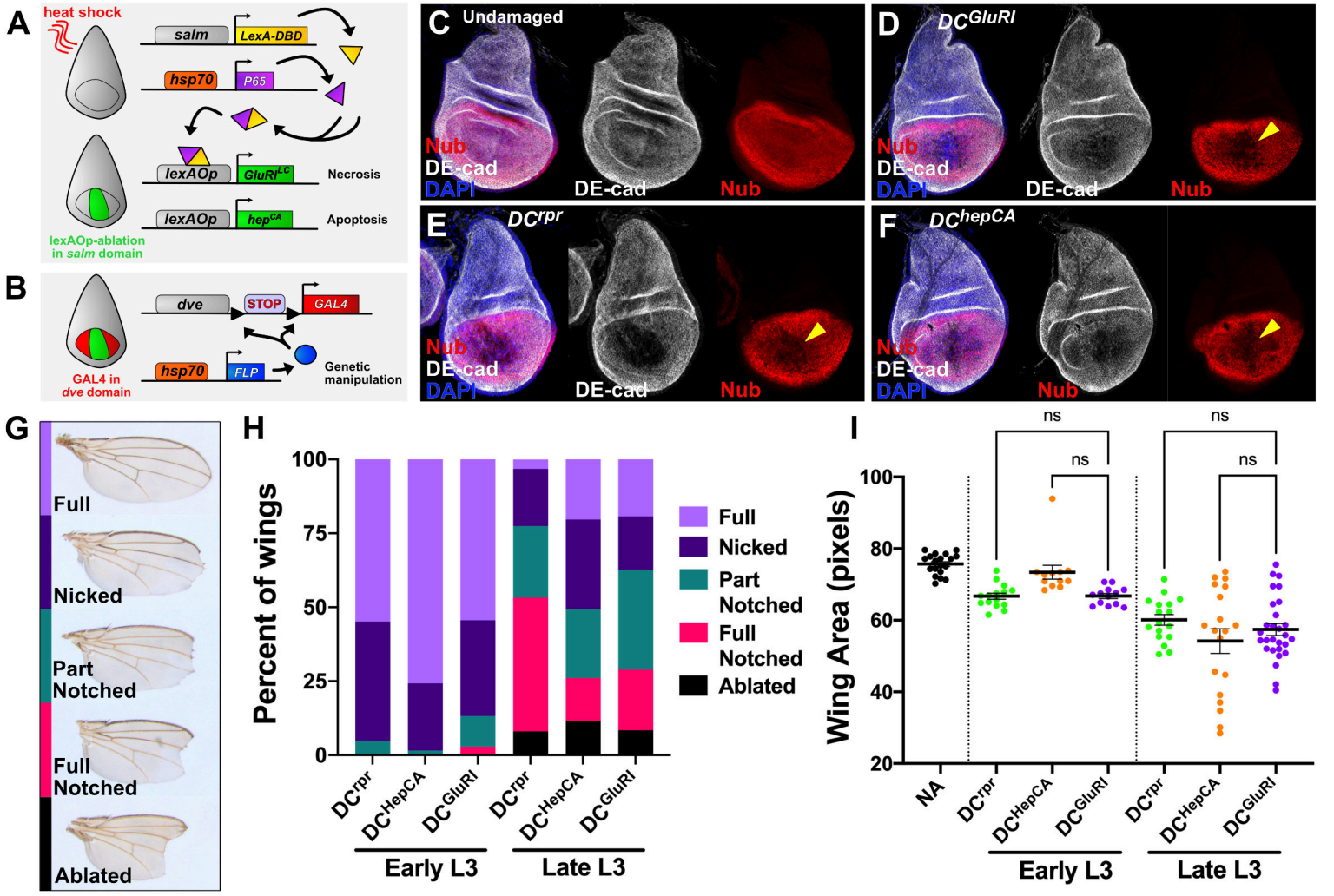
A
heat shock
salm
LexA-DBD
hsp70
P65
lexAOp
GluRI^LC
Necrosis
lexAOp
hep^CA
Apoptosis
lexAOp-ablation in salm domain
B
dve
STOP
GAL4
hsp70
FLP
Genetic manipulation
GAL4 in dve domain
C Undamaged
D DC^GluRI
E DC^rpr
F DC^hepCA
Nub
DE-cad
DAPI
G
Full
Nicked
Part Notched
Full Notched
Ablated
H
Percent of wings
100
75
50
25
0
Full
Nicked
Part Notched
Full Notched
Ablated
DC^rpr
DC^HepCA
DC^GluRI
Early L3
Late L3
I
Wing Area (pixels)
100
80
60
40
20
ns
NA
DC^rpr
DC^HepCA
DC^GluRI
Early L3
Late L3

710 **Figure Legends**

711 **Figure 1. *Drosophila* wing imaginal discs regenerate comparably following**

712 **ablation with DC^{rpr}, DC^{hepCA} and DC^{GluR1}.**

713 (**A-B**) A schematic of the DUAL Control genetic ablation system. This system is based

714 on a split LexA transcriptional activator which can form a complete transcriptional

715 activator (yellow/purple protein) using complementary leucine zipper domains following

716 a heat shock. This in turn induces *lexAOp*-driven ablation in the *salm* domain (green

717 area of disc) (**A**). The *DVE>>GAL4* driver is used to drive *UAS*-based transgenes in the

718 wing pouch independent of ablation (red area of disc), following the removal of a stop

719 cassette by *hs-Flp* (**B**). Red lines in (**A**) indicate a heat shock. *salm*: *spalt* enhancer,

720 *DBD: DNA Binding Domain*, *dve*: *defective proventriculus* enhancer, *Flp: Flp*

721 *recombinase*.

722 (**C-F**) Wing discs stained for the Nubbin pouch marker (Nub, red) and DE-cadherin (DE-

723 cad, gray) in an unablated control (DC^{NA}) (**C**) and following ablation with DC^{GluR1} (**D**),

724 DC^{rpr} (**E**), and DC^{hepCA} (**F**). DAPI, blue. Arrowheads in (**D-F**) indicate loss of Nub pouch

725 marker.

726 (**G**) Adult wing ablation phenotypes following DUAL Control ablation (see also Harris et

727 al., 2020).

728 (**H**) Regeneration scoring of adult wings from early L3 discs ablated by DC^{rpr} (n = 62),

729 DC^{hepCA} (n = 66), and DC^{GluR1} (n = 68), and late L3 discs ablated by DC^{rpr} (n = 62),

730 DC^{hepCA} (n = 69), and DC^{GluR1} (n = 83).

731 (**I**) Mean pixel area of adult wings from early L3 ablated wings in an unablated control

732 (NA, n = 19), DC^{rpr} (n = 22), DC^{hepCA} (n = 12), and DC^{GluR1} (n = 17). ns, not significant.

733 Data analyzed using one-factor ANOVA and Tukey's multiple comparisons test.

734

Figure 2

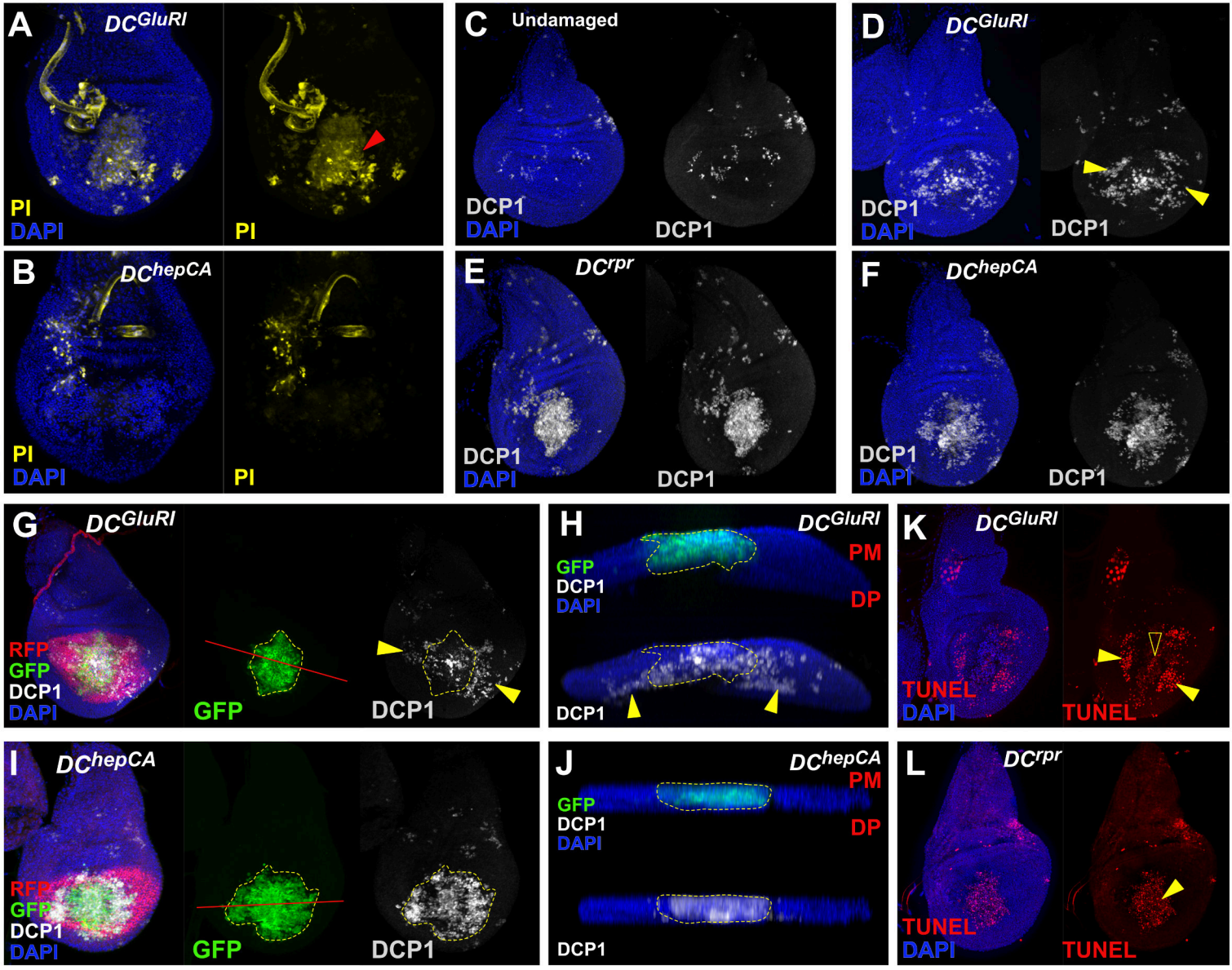
A
DCGluRI
PI
DAPI
PI
B
DChepCA
PI
DAPI
PI
C
Undamaged
DCP1
DAPI
DCP1
D
DCGluRI
DCP1
DAPI
DCP1
E
DCrpr
DCP1
DAPI
DCP1
F
DChepCA
DCP1
DAPI
DCP1
G
DCGluRI
RFP
GFP
DCP1
DAPI
GFP
DCP1
H
DCGluRI
GFP
DCP1
DAPI
PM
DP
DCP1
K
DCGluRI
TUNEL
DAPI
TUNEL
I
DChepCA
RFP
GFP
DCP1
DAPI
GFP
DCP1
J
DChepCA
GFP
DCP1
DAPI
PM
DP
DCP1
L
DCrpr
TUNEL
DAPI
TUNEL

735 **Figure 2: Ablation with *DC^{GluR1}* generates apoptosis at a distance.**

736 (**A-B**) Propidium iodide (PI) staining (yellow) of *DC^{GluR1}* (**A**) and *DC^{hepCA}* (**B**) ablated
737 wing discs. Arrowhead in (**A**) indicates PI-stained dying cells in the *salm* domain of the
738 pouch. Non-specific PI staining of tracheal tubes is observed in both samples. DAPI,
739 blue.

740 (**C-F**) Caspase staining (DCP1, gray) of wing imaginal discs in an unablated control (**C**),
741 and following ablation with *DC^{GluR1}* (**D**), *DC^{rpr}* (**E**), and *DC^{hepCA}* (**F**). DAPI, blue.
742 Arrowheads in (**D**) indicate non-autonomous caspase outside of the ablation domain.

743 (**G-J**) Wing imaginal discs bearing the *lexAop-GFP; UAS-RFP* reporter and ablated with
744 *DC^{GluR1}* (**G-H**) or *DC^{hepCA}* (**I-J**). GFP (green) labels the *salm* ablation domain, RFP (red)
745 labels the surrounding unablated pouch, and DCP1 (gray) labels apoptotic cells. DAPI,
746 blue. (**G**) Discs ablated with *DC^{GluR1}* shows DCP1-positive cells outside of the ablation
747 domain (arrowheads), red line indicates transverse section shown in (**H**). (**H**) A
748 transverse section through the pouch of the disc in (**G**) confirms that these lateral
749 DCP1-positive cells are not labeled with GFP. (**I**) Ablation by *DC^{hepCA}* shows almost
750 complete overlap between the GFP and DCP1 signals, red line indicates transverse
751 section shown in (**J**). (**J**) A transverse section of the disc in (**I**) confirming significant
752 overlap of GFP and DCP1. PM: peripodial membrane, DP: disc proper.

753 (**K-L**) TUNEL-labeling (red) of wing discs ablated with *DC^{GluR1}* (**K**) and *DC^{rpr}* (**L**). Solid
754 arrowheads indicate strong TUNEL staining in both panels, open arrowhead in (**K**)
755 indicates weak TUNEL staining present in the *salm* domain.

756

Figure 3

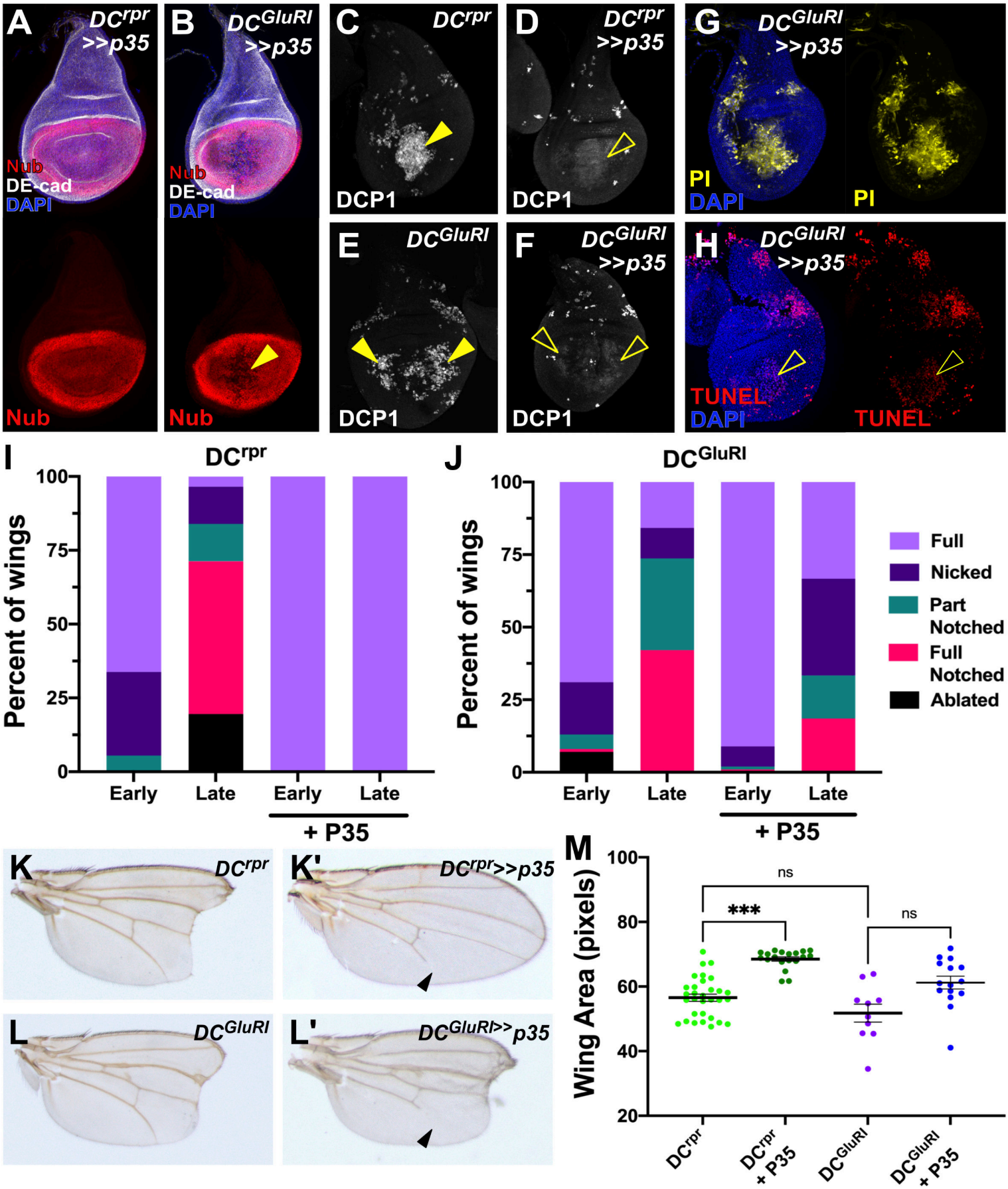
A
DCrpr >>p35
Nub
DE-cad
DAPI
Nub
B
DCGluRI >>p35
Nub
DE-cad
DAPI
Nub
C
DCrpr
DCP1
D
DCrpr >>p35
DCP1
G
DCGluRI >>p35
PI
DAPI
PI
E
DCGluRI
DCP1
F
DCGluRI >>p35
DCP1
H
DCGluRI >>p35
TUNEL
DAPI
TUNEL
I
DCrpr
Percent of wings
100
75
50
25
0
Early
Late
Early
Late
+ P35
J
DCGluRI
Percent of wings
100
75
50
25
0
Early
Late
Early
Late
+ P35
Full
Nicked
Part Notched
Full Notched
Ablated
K
DCrpr
K'
DCrpr>>p35
L
DCGluRI
L'
DCGluRI>>p35
M
Wing Area (pixels)
100
80
60
40
20
ns
***
ns
DCrpr
DCrpr + P35
DCGluRI
DCGluRI + P35

757 **Figure 3. Inhibition of caspase activity fails to prevent ablation in DC^{GluR1} discs.**

758 (**A-B**) Wing discs stained for Nub (red) and DE-cad (gray) following ablation with

759 *DC^{rpr}>>p35* (**A**) and *DC^{GluR1}>>p35* (**B**). DAPI, blue. Loss of tissue by *DC^{GluRI}* ablation in

760 the presence of P35 is indicated by the arrowhead in (**B**).

761 (**C-F**) DCP1 staining (gray) in wing discs ablated with *DC^{rpr}* (**C**), *DC^{rpr}>>p35* (**D**), *DC^{GluR1}*

762 (**E**), *DC^{GluR1}>>p35* (**F**). The arrowheads indicate strong DCP1 staining in the ablated

763 *salm* domain in (**C**) and non-autonomous apoptosis in (**E**), while the open arrowheads in

764 (**B**) and (**F**) indicate the diffuse, cytoplasmic DCP1 staining in these populations that

765 occurs in the presence of P35.

766 (**G**) PI staining (yellow) of a *DC^{GluR1}>>p35* ablated wing disc. Non-specific PI staining of

767 the tracheal tube is observed. DAPI, blue.

768 (**H**) TUNEL-labeling (red) of a *DC^{GluR1}>>p35* ablated wing disc. DAPI, blue. The open

769 arrowhead indicates weak TUNEL staining in the *salm* domain, while the lateral TUNEL

770 staining is no longer observed in the presence of P35.

771 (**I-J**) Regeneration scoring of adult wings from early and late L3 discs ablated by *DC^{rpr}*

772 (**I**) or *DC^{GluR1}* (**J**) in the presence and absence of P35. Number of wings scored: early

773 and late L3 *DC^{rpr}* (n = 74, n = 87), early and late L3 *DC^{rpr}>>p35* (n = 110, n = 125), early

774 and late L3 *DC^{GluRI}* (n = 100, n = 38), early and late L3 *DC^{GluRI}>>p35* (n = 101, n = 27).

775 (**K-L'**) Adult wing phenotypes following ablation with *DC^{rpr}* (**K**), *DC^{rpr}>>p35* (**K'**), *DC^{GluR1}*

776 (**L**), and *DC^{GluR1}>>p35* (**L'**). Arrowheads in (**K'**) and (**L'**) indicate an incomplete L5 vein,

777 which is a consequence of *p35* expression on vein development, reported previously

778 (Perez-Garijo et al. 2004).

779 (**M**) The mean area of adult wings from discs ablated with *DC*^{rpr} (n = 31), *DC*^{rpr}*>>p35* (n

780 = 19), *DC*^{GluR1} (n = 10), and *DC*^{GluR1}*>>p35* (n = 15), ns, not significant, *** p = 0.0002,

781 data analyzed by one-factor ANOVA and Tukey's multiple comparisons test.

782

Figure 4

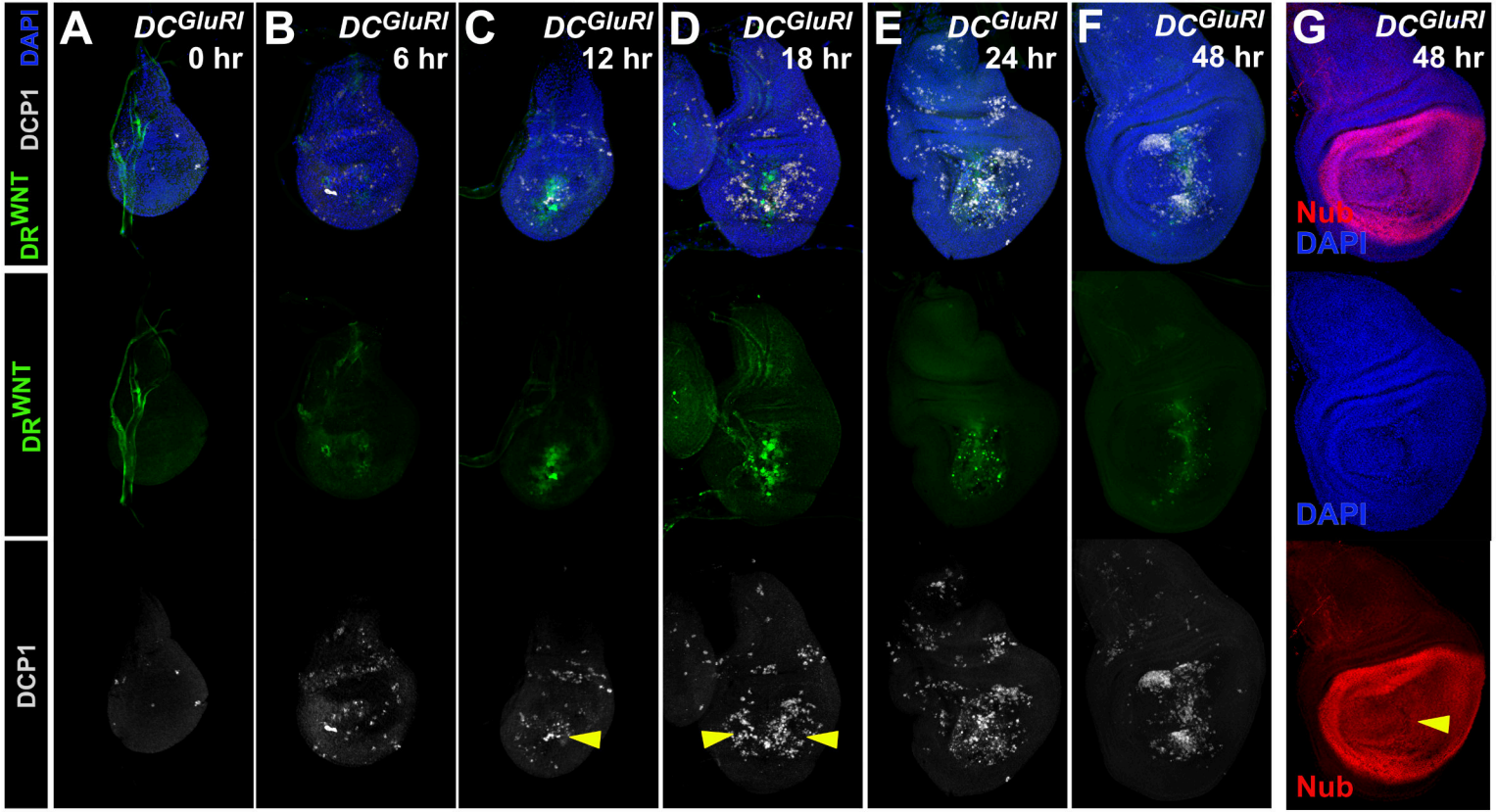
DR^WNT DCP1 DAPI
DR^WNT
DCP1
A DC^GluRI 0 hr
B DC^GluRI 6 hr
C DC^GluRI 12 hr
D DC^GluRI 18 hr
E DC^GluRI 24 hr
F DC^GluRI 48 hr
G DC^GluRI 48 hr
Nub
DAPI
DAPI
Nub

783 **Figure 4. Necrosis-induced apoptosis (NiA) forms after wound edge signaling**

784 **occurs.**

785 (**A-F**) A time course of regeneration for wing discs bearing a fluorescent reporter of a

786 damage-responsive WNT enhancer (*DR*^{WNT}, green, (Harris et al. 2016) ablated with

787 *DC*^{GluR1} and stained for DCP1 (gray) at (**A**) 0 hr, (**B**) 6 hr, (**C**) 12 hr, (**D**) 18 hr, (**E**) 24 hr,

788 (**F**) 48 hr after heat shock. DAPI, blue. Arrowhead in (**C**) indicates wound edge

789 apoptosis at 6 hr coinciding with the appearance of *DR*^{WNT} expression, arrowheads in

790 (**D**) indicates NiA at 18 hr.

791 (**G**) A wing imaginal disc at 48 hr of recovery following ablation with *DC*^{GluR1}. The pouch

792 marker Nub (red) and DAPI staining (blue) show continuity of the pouch is restored

793 (arrowhead).

794

Figure 5

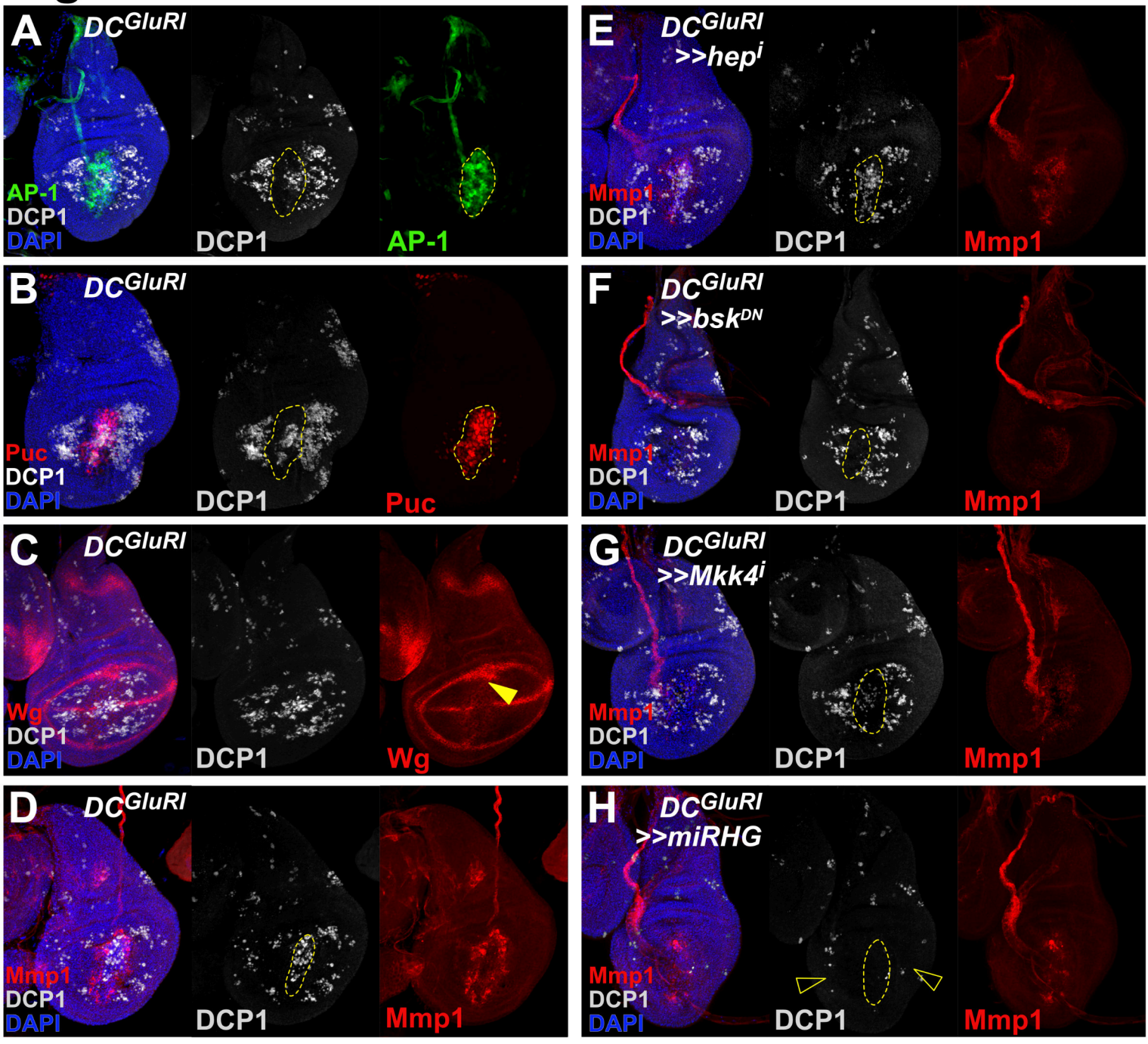
A
DC^GluRI
AP-1
DCP1
DAPI
DCP1
AP-1
B
DC^GluRI
Puc
DCP1
DAPI
DCP1
Puc
C
DC^GluRI
Wg
DCP1
DAPI
DCP1
Wg
D
DC^GluRI
Mmp1
DCP1
DAPI
DCP1
Mmp1
E
DC^GluRI
>>hep^i
Mmp1
DCP1
DAPI
DCP1
Mmp1
F
DC^GluRI
>>bsk^DN
Mmp1
DCP1
DAPI
DCP1
Mmp1
G
DC^GluRI
>>Mkk4^i
Mmp1
DCP1
DAPI
DCP1
Mmp1
H
DC^GluRI
>>miRHG
Mmp1
DCP1
DAPI
DCP1
Mmp1

795 **Figure 5. Necrosis-induced apoptosis (NiA) acts independent of the JNK pathway.**

796 (**A-B**) Wing discs ablated with *DC*^{GluR1} and bearing the *AP-1-GFP* (green) (**A**) and *puc-*

797 *lacZ* (red) (**B**) reporters of JNK pathway activity, stained for DCP1 (gray). DAPI, blue.

798 These reporters show strong overlap with the wound edge apoptosis, but not with the

799 NiA cells. As in other panels, the dashed line outlines the ablated *salm* domain,

800 indicated by the appearance of cells labeled by DAPI.

801 (**C-D**) Wing imaginal discs ablated with *DC*^{GluR1} and stained for the JNK targets Wg

802 (red) (**C**) and Mmp1 (red) (**D**). Arrowhead in (**C**) indicates ectopic Wg at the wound

803 edge. DCP1, gray; DAPI, blue.

804 (**E**) A wing imaginal disc ablated with *DC*^{GluR1}*>>hep*^{RNAi} stained for DCP1 (gray) and

805 Mmp1 (red), DAPI, blue. Both the wound edge apoptosis and NiA cells remain

806 unaffected following knockdown of *hep*.

807 (**F**) A wing imaginal disc ablated with *DC*^{GluR1}*>>bsk*^{DN} stained for DCP1 (gray) and

808 Mmp1 (red). DAPI, blue. Wound edge apoptosis is largely absent, while NiA cells

809 remain unaffected.

810 (**G**) A wing imaginal disc ablated with *DC*^{GluR1}*>>Mkk4*^{RNAi} stained for DCP1 (gray) and

811 Mmp1 (red). DAPI, blue. Wound edge apoptosis is strongly reduced, while NiA cells

812 remain unaffected.

813 (**H**) A wing imaginal disc ablated with *DC*^{GluR1}*>>miRHG* stained for DCP1 (gray) and

814 Mmp1 (red). DAPI, blue. Both the wound edge apoptosis and NiA (open arrowheads)

815 are eliminated following knockdown of *rpr, hid,* and *grim* with *miRHG*.

816

Figure 6

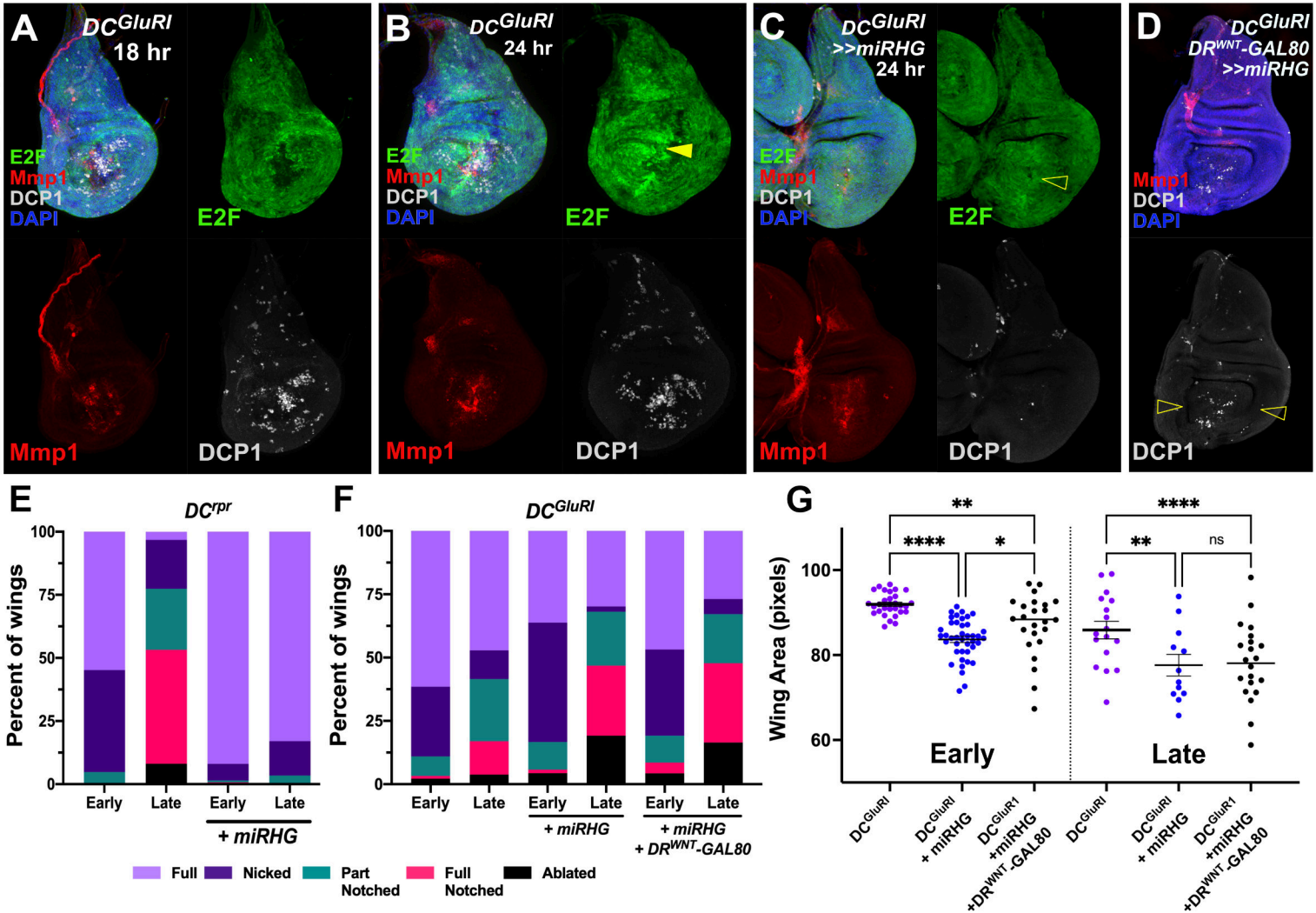
A
DC^GluRI
18 hr
E2F
Mmp1
DCP1
DAPI
E2F
Mmp1
DCP1
B
DC^GluRI
24 hr
E2F
Mmp1
DCP1
DAPI
E2F
Mmp1
DCP1
C
DC^GluRI
>>miRHG
24 hr
E2F
Mmp1
DCP1
DAPI
E2F
Mmp1
DCP1
D
DC^GluRI
DR^WNT-GAL80
>>miRHG
Mmp1
DCP1
DAPI
DCP1
E
DC^rpr
Percent of wings
100
75
50
25
0
Early
Late
Early
Late
+ miRHG
F
DC^GluRI
Percent of wings
100
75
50
25
0
Early
Late
Early
Late
+ miRHG
Early
Late
+ miRHG
+ DR^WNT-GAL80
Full
Nicked
Part Notched
Full Notched
Ablated
G
Wing Area (pixels)
100
80
60
**
****
*
****
**
ns
Early
Late
DC^GluRI
DC^GluRI + miRHG
DC^GluR1 +miRHG +DR^WNT-GAL80
DC^GluRI
DC^GluRI + miRHG
DC^GluR1 +miRHG +DR^WNT-GAL80

817 **Figure 6. Blocking NiA formation impairs regeneration.**

818 (**A-B**) Wing discs bearing an *E2F* transcriptional reporter (*PCNA-GFP,* green) ablated
819 with DC^{GluR1} and stained for Mmp1 (red) and DCP1 (gray) at 18 hr (**A**) and 24 hr (**B**) of
820 recovery. DAPI, blue. Arrowhead in (**B**) shows the localized proliferation that is only
821 present after 24 hr of recovery.

822 (**C**) Wing disc bearing *PCNA-GFP* (green) ablated with DC^{GluR1}*>>miRHG* and stained
823 for Mmp1 (red) and DCP1 (gray), DAPI, blue. The open arrowhead indicates reduced
824 proliferation upon *miRHG* expression. JNK signaling, indicated by Mmp1 staining, is still
825 present in these discs.

826 (**D**) A wing imaginal disc ablated by DC^{GluR1}*>>miRHG* in the presence of DR^{WNT}*-GAL80*
827 and stained for DCP1 (gray) and Mmp1 (red). DAPI, blue. Open arrowheads indicate a
828 loss of NiA.

829 (**E-F**) Regeneration scoring of adult wings from early and late L3 discs ablated with
830 DC^{rpr} (**E**) or DC^{GluR1} (**F**) in the presence and absence of *miRHG*. Number of wings
831 scored: early and late L3 DC^{rpr} (n = 62, n = 63), early and late L3 DC^{rpr}*>>miRHG* (n =
832 137, n = 88), early and late L3 DC^{GluRI} (n = 91, n = 53), early and late L3
833 DC^{Glu1r}*>>miRHG* (n = 138, n = 47), and early and late L3 DC^{GluR1}*>> miRHG,* DR^{WNT}-
834 *GAL80* (n = 47, n = 67). While *miRHG* leads to more full and nicked wings following
835 DC^{rpr} ablation, the opposite is seen following DC^{GluR1} ablation and DC^{GluR1}
836 +DR^{WNT}*-GAL80*.

837 (**G**) Mean pixel area of adult wings from early and late L3 discs ablated with DC^{GluR1}
838 (early n = 30, late n = 17), DC^{GluR1}*>>miRHG* (early n = 41, late n = 12), and DC^{GluR1}*>>*
839 *miRHG,* DR^{WNT}*-GAL80* (early n = 24, late n = 22). ns: not significant, ** p = 0.0056

840 (early DC^{GluRI} vs. DC^{GluRI} + *miRHG* + DR^{WNT}-*GAL80*), **** p <0.0001, * p =0.0254, ** p =

841 0.0015 (late DC^{GluRI} vs. DC^{GluRI} + *miRHG*), data analyzed by one-factor ANOVA and

842 FDR's multiple comparisons tests.

843

Figure 7

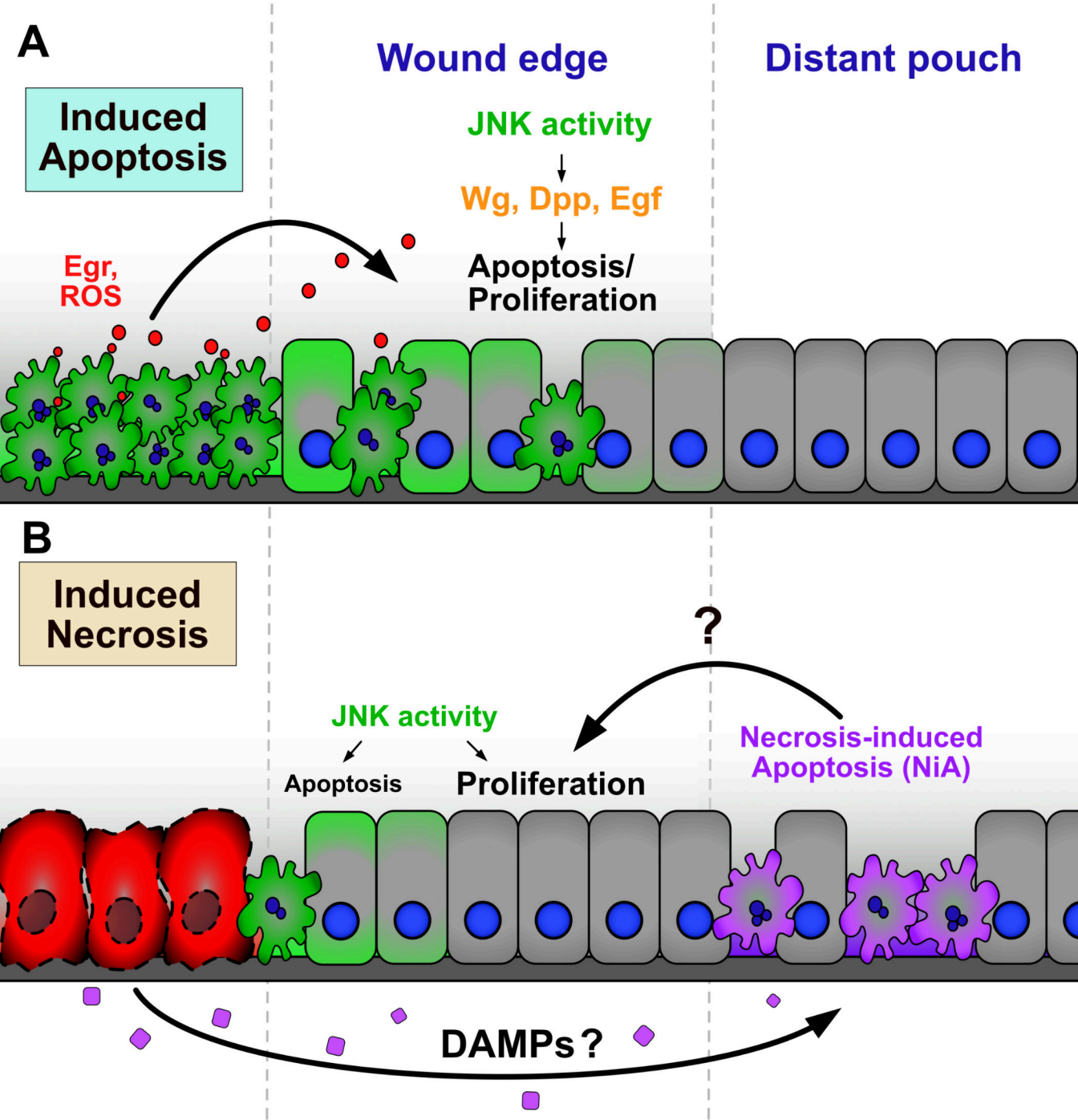
A
Wound edge
Distant pouch
Induced Apoptosis
JNK activity
Wg, Dpp, Egf
Apoptosis/ Proliferation
Egr, ROS
B
Induced Necrosis
?
JNK activity
Apoptosis
Proliferation
Necrosis-induced Apoptosis (NiA)
DAMPs ?

844 **Figure 7. NiA cells promotes regeneration in *DC^{GluR1}* ablated discs**

845 (**A-B**) Schematics depicting the cell signaling events that occur resulting from apoptotic
846 ablation (**A**) and necrotic ablation (**B**). Previous studies have shown dying cells release
847 reactive oxygen species (ROS) and promote Egr release via hemocytes and potentially
848 other mechanisms, inducing high levels of JNK signaling at the wound edge (Fogarty
849 and Bergmann 2017). In turn, wound edge apoptotic cells and surviving cells with lower
850 JNK signaling release mitogens including Wg, Dpp, and Egf, to promote regenerative
851 signaling in the adjacent wound edge tissue. In cells undergoing necrosis, low levels of
852 JNK signaling occurs downstream of the receptor at the wound edge, likely through
853 pathways related to polarity disruption, mechanical stress, or immediate stress signals
854 such as ROS. This signaling induces sporadic apoptosis at the wound edge that
855 potentially contributes to proliferation and recovery. Necrotic cells also release an as yet
856 unidentified long-range signal that could be a damage associated molecular pattern
857 (DAMP), resulting in the formation of NiA cells in the distant pouch. These cells promote
858 proliferation formation and regeneration.

Figure S1

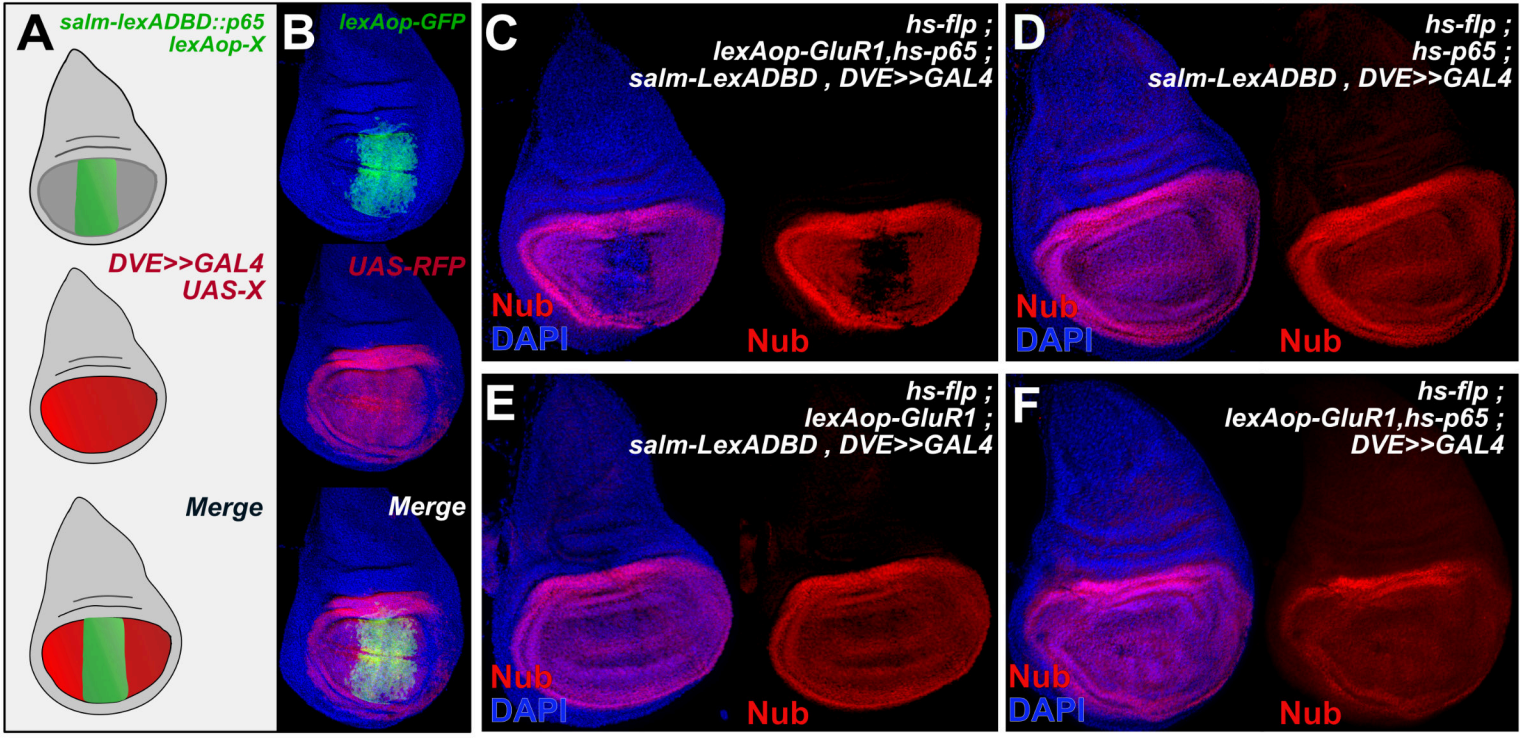
A
salm-lexADBD::p65
lexAop-X
DVE>>GAL4
UAS-X
Merge
B
lexAop-GFP
UAS-RFP
Merge
C
hs-flp ;
lexAop-GluR1,hs-p65 ;
salm-LexADBD , DVE>>GAL4
Nub
DAPI
Nub
D
hs-flp ;
hs-p65 ;
salm-LexADBD , DVE>>GAL4
Nub
DAPI
Nub
E
hs-flp ;
lexAop-GluR1 ;
salm-LexADBD , DVE>>GAL4
Nub
DAPI
Nub
F
hs-flp ;
lexAop-GluR1,hs-p65 ;
DVE>>GAL4
Nub
DAPI
Nub

Supplemental Figure Legends

Figure S1. Related to Figure 1

Ablation and gene expression using DUAL Control

(**A**) A schematic of the domains used for ablation and genetic manipulation in most DUAL Control experiments. The ablation domain coincides with an enhancer of the *salm* gene, which patterns the distal wing pouch. The domain used for genetic manipulation utilizes an enhancer of the *dve* gene, which drives *UAS*-based constructs in the entire wing pouch.

(**B**) A wing imaginal disc bearing DC^{NA} with *lexAop-GFP* to mark the ablation domain (green) and *UAS-RFP* to mark the pouch domain (red), as diagrammed in the schematic in (**A**). DAPI, blue.

(**C**-**F**) Wing discs bearing combinations of the transgenes that comprise DUAL Control, showing that heat shock induced ablation only occurs when all three genes (*hsp65, lexAop-GluRI, salm-LexADBD*) are present, as indicated by the presence of Nub (red) in the *salm* domain. DAPI, blue. Genes omitted: (**D**) *lexAop-GluR1* (**E**) *hs-p65* (**F**) *salm-LexADBD.*

Figure S2

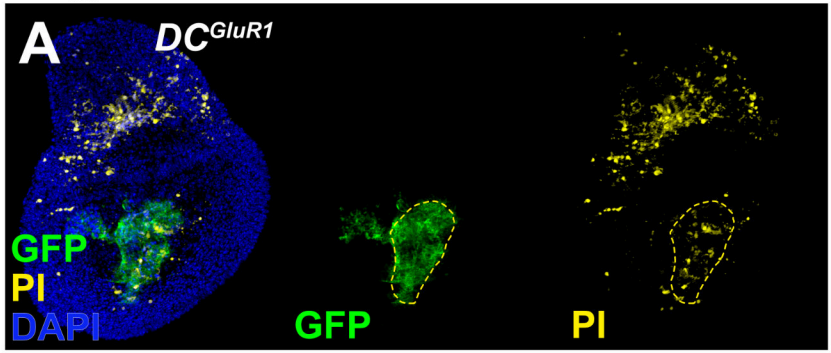
A
DCGluR1
GFP
PI
DAPI
GFP
PI

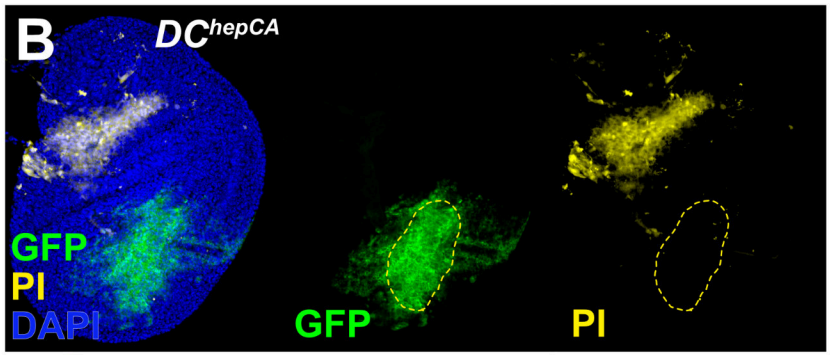
B
DChepCA
GFP
PI
DAPI
GFP
PI

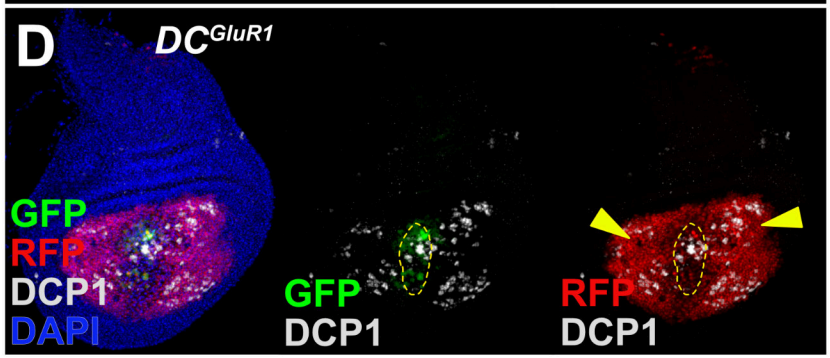
D
DCGluR1
GFP
RFP
DCP1
DAPI
GFP
DCP1
RFP
DCP1

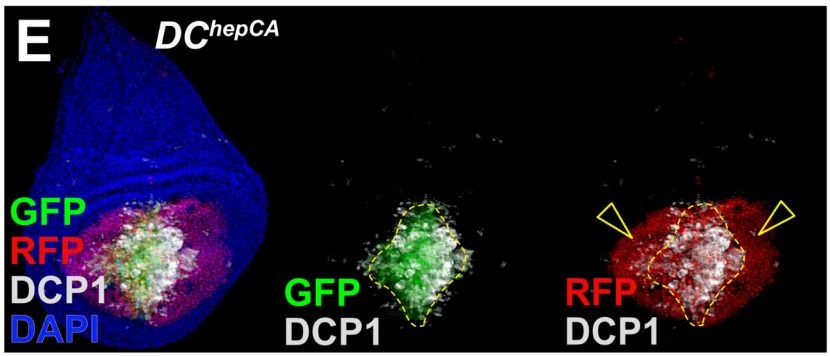
E
DChepCA
GFP
RFP
DCP1
DAPI
GFP
DCP1
RFP
DCP1

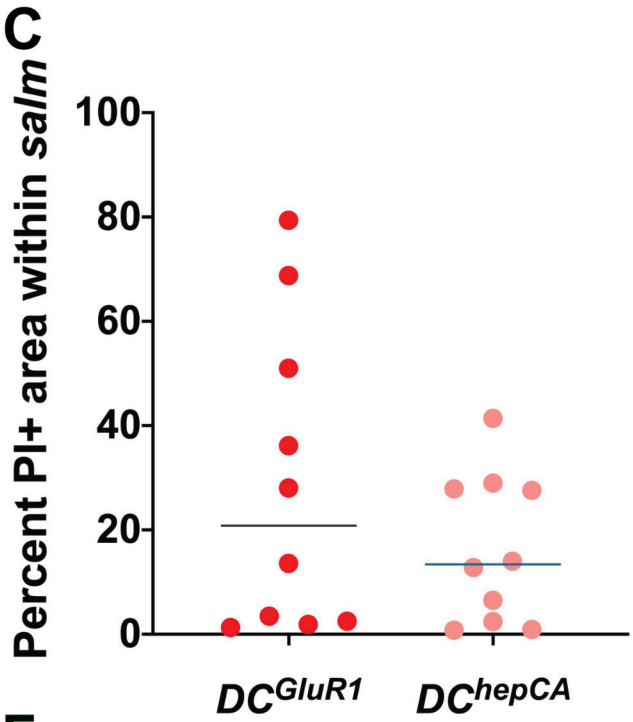
C
Percent PI+ area within salm
100
80
60
40
20
0
DCGluR1
DChepCA

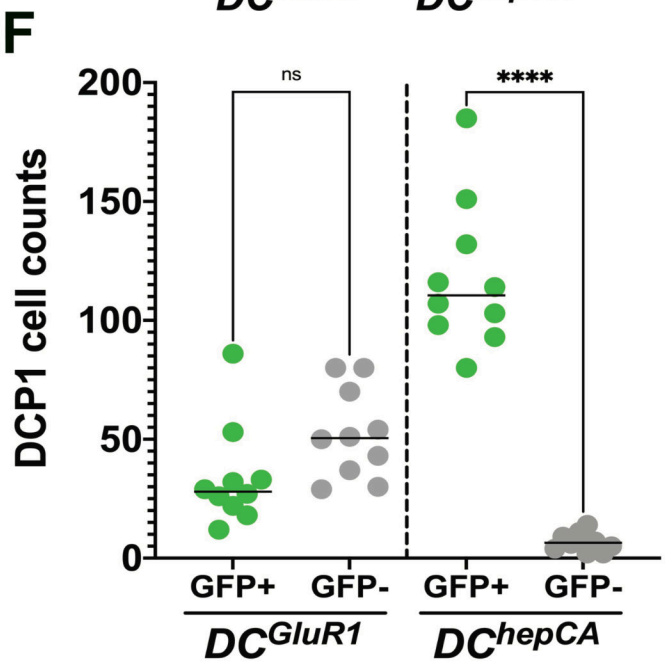
F
DCP1 cell counts
200
150
100
50
0
ns
****
GFP+
GFP-
GFP+
GFP-
DCGluR1
DChepCA

Figure S2. Related to Figure 2

Quantification of cell death in GluRI ablated discs

(**A**-**B**) Wing discs bearing a *lexAop-GFP* transgene and ablated with DC^{GluR1} (**A**) and DC^{hepCA} (**B**) and stained for PI (yellow). DAPI, blue. PI staining in the notum is due to physical manipulation of the wing discs and acts as an internal control.

(**C**) Quantification of the PI signal. The *lexAop-GFP* was used to outline the ablated tissue for quantification, as seen in (A) and (B). n = 10 discs for each treatment.

(**D**-**E**) Wing imaginal discs bearing a DR^{WNT}*-GFP ; UAS-RFP* transgene, ablated with DC^{GluR1} (**D**) and DC^{hepCA} (**E**), and stained for DCP1, gray. DAPI, blue. Solid arrowheads in (D) highlight GFP negative, DCP1 positive cells. Open arrowheads in (E) indicate a lack of GFP negative, DCP1 positive cells in DC^{hepCA} ablated discs.

(**F**). Quantification of DCP1 cells at the wound edge (GFP+) vs. the lateral wing pouch (GFP-). ns: not significant. P**** < 0.0001. Data analyzed with a Kruskal-Wallis test and a Tukey's multiple comparisons test. n = 10 discs for each treatment.

Figure S3

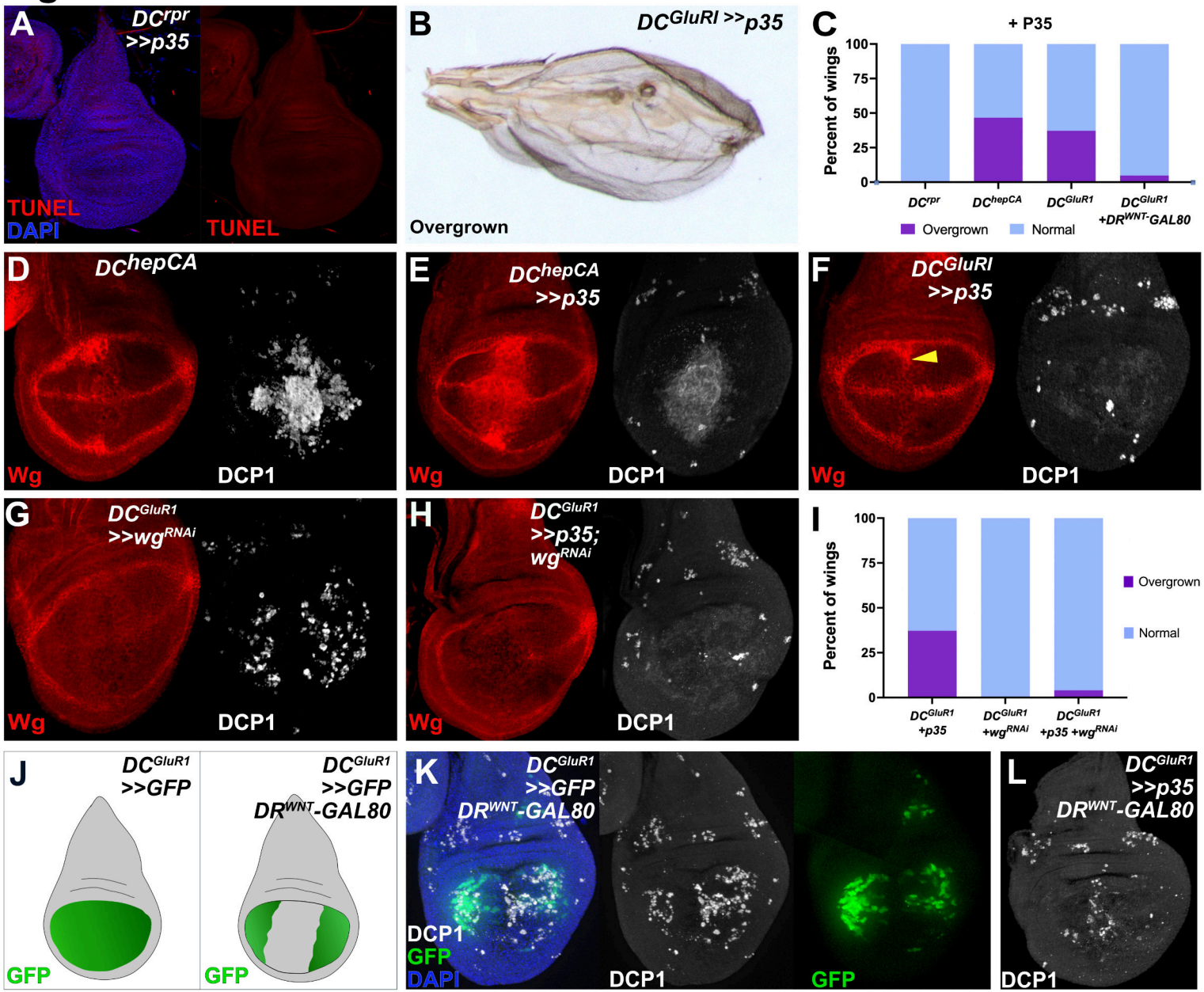
A
DCrpr >>p35
TUNEL
DAPI
TUNEL
B
DCGluRI >>p35
Overgrown
C
+ P35
Percent of wings
100
75
50
25
0
DCrpr
DChepCA
DCGluR1
DCGluR1 +DRWNT-GAL80
Overgrown
Normal
D
DChepCA
Wg
DCP1
E
DChepCA >>p35
Wg
DCP1
F
DCGluRI >>p35
Wg
DCP1
G
DCGluR1 >>wgRNAi
Wg
DCP1
H
DCGluR1 >>p35; wgRNAi
Wg
DCP1
I
Percent of wings
100
75
50
25
0
DCGluR1 +p35
DCGluR1 +wgRNAi
DCGluR1 +p35 +wgRNAi
Overgrown
Normal
J
DCGluR1 >>GFP
GFP
DCGluR1 >>GFP DRWNT-GAL80
GFP
K
DCGluR1 >>GFP DRWNT-GAL80
DCP1
GFP
DAPI
DCP1
GFP
L
DCGluR1 >>p35 DRWNT-GAL80
DCP1

Figure S3. Related to Figure 3

Blocking apoptosis with P35 leads to wing overgrowth phenotypes

(**A**) A wing disc ablated with *DC^{rpr}>>p35* and labeled with TUNEL (red). DAPI, blue. The lack of signal demonstrates the ability of P35 to inhibit cell death.

(**B**) Adult wings showing the overgrown phenotype accompanied by blistering and ectopic vein tissue observed following *DC^{GluR1}>>p35* ablation.

(**C**) Quantification of overgrown wing phenotype frequency following ablation with *DC^{rpr}>>p35* (n = 89), *DC^{hepCA}>>p35* (n = 30), *DC^{GluR1}>>p35* (n = 43), and *DC^{GluR1} DR^{Wnt}-GAL80 >>p35* (104). No overgrown wings are observed in *DC^{rpr}>>p35*.

(**D-F**) Wing imaginal discs stained for Wg (red) and DCP1 (gray) following ablation with *DC^{hepCA}* (**D**), *DC^{hepCA}>>p35* (**E**) or *DC^{GluR1}>>p35* (**F**). Ectopic Wg overlaps with the diffuse DCP1 signal in *DC^{hepCA}>>p35* discs, while in *DC^{GluR1}>>p35* discs ectopic Wg is only observed at the wound edge (arrowhead) and not in the diffuse DCP1 signal in the rest of the pouch.

(**G-H**) Wing imaginal discs ablated with *DC^{GluR1}>>wg^{RNAi}* (**G**) *DC^{GluR1}>>p35; wg^{RNAi}* (**H**) and stained for Wg (red) and DCP1 (gray).

(**I**) Quantification of overgrown wing phenotype frequency following ablation with *DC^{GluR1}* (n = 43), *DC^{GluR1}>>^{wgRNAi}* (n = 62), and *DC^{GluR1}>>p35; wg^{RNAi}* (n = 46).

(**J**) Schematic of wing discs bearing *DC^{GluR1}>>GFP* with and without *DR^{WNT}-GAL80*, demonstrating the ability of *DR^{WNT}-GAL80* to limit *UAS-GFP* expression to the lateral pouch.

(**K**) A wing disc ablated by *DC*^{GluR1}*>>GFP , DR*^{Wnt}*-GAL80* and stained for DCP1 (gray). DAPI, blue. The GFP signal overlaps with the NiA cells but not the wound edge apoptosis.

(**L**) A wing disc ablated by *DC*^{GluR1}*>>p35 , DR*^{Wnt}*-GAL80* and stained for DCP1 (gray). DAPI, blue. The wound edge DCP1 is still strong and punctate while the NiA cells are no longer visible.

Figure S4

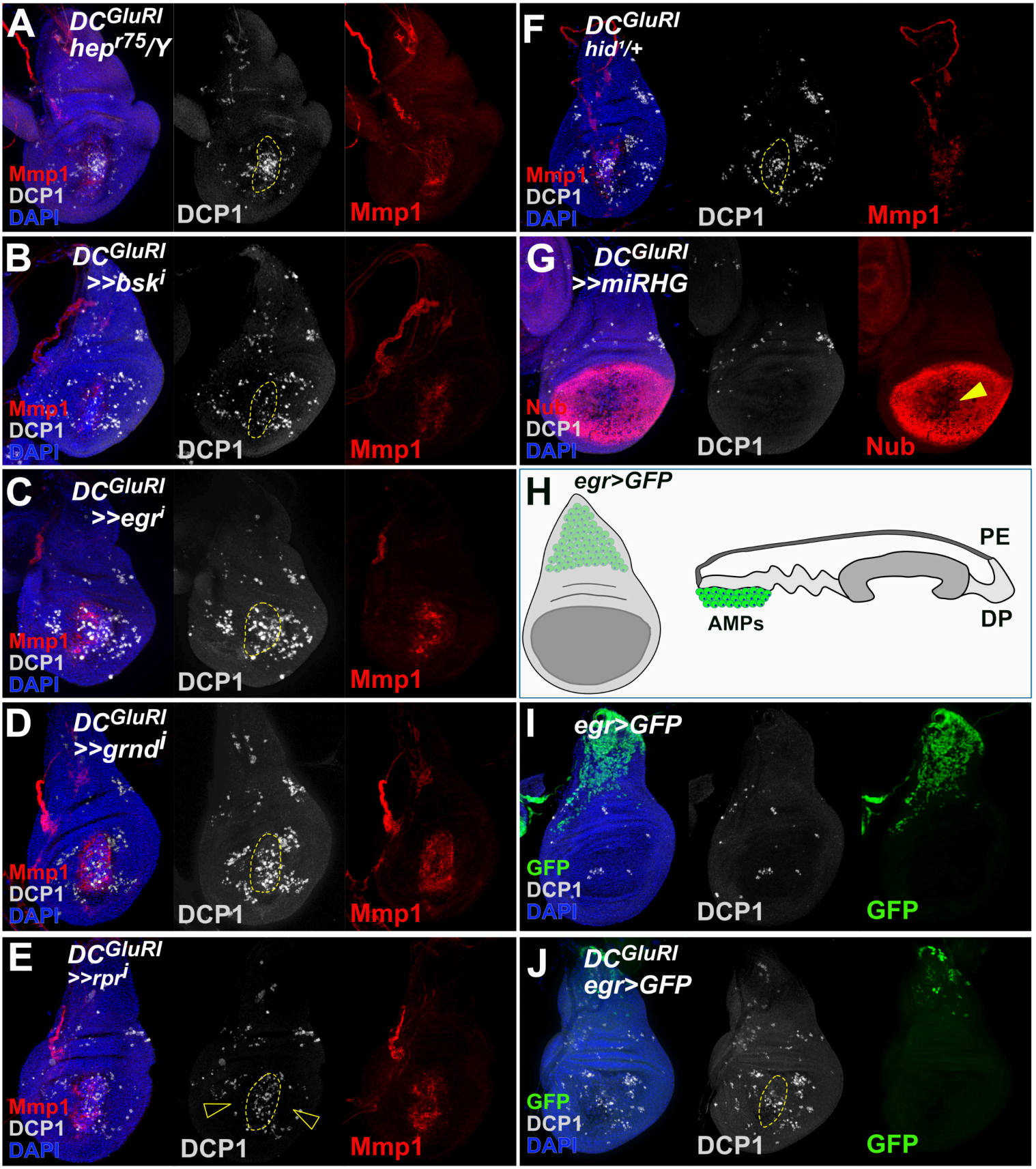
A
DC^GluRI
hep^r75/Y
Mmp1
DCP1
DAPI
DCP1
Mmp1
B
DC^GluRI
>>bsk^i
Mmp1
DCP1
DAPI
DCP1
Mmp1
C
DC^GluRI
>>egr^i
Mmp1
DCP1
DAPI
DCP1
Mmp1
D
DC^GluRI
>>grnd^i
Mmp1
DCP1
DAPI
DCP1
Mmp1
E
DC^GluRI
>>rpr^i
Mmp1
DCP1
DAPI
DCP1
Mmp1
F
DC^GluRI
hid^1/+
Mmp1
DCP1
DAPI
DCP1
Mmp1
G
DC^GluRI
>>miRHG
Nub
DCP1
DAPI
DCP1
Nub
H
egr>GFP
PE
AMPs
DP
I
egr>GFP
GFP
DCP1
DAPI
DCP1
GFP
J
DC^GluRI
egr>GFP
GFP
DCP1
DAPI
DCP1
GFP

Figure S4. Related to Figure 5.

Manipulation of JNK pathway elements in *DC^{GluRI}* ablated discs.

(**A**) A wing disc ablated with *DC^{GluR1}* in a *hep^{r75}* hemizygous background and stained for DCP1 (gray) and Mmp1 (red). DAPI, blue. Wound edge apoptosis and NiA cells are still observed in this background, although are overall reduced. As in other panels, the dashed line outlines the ablated *salm* domain, indicated by the change in DAPI appearance.

(**B**) A wing disc ablated with *DC^{GluR1}>>bsk^{RNAi}* and stained for DCP1 (gray) and Mmp1 (red), DAPI, blue. Wound edge apoptotic cells are reduced following *bsk* knockdown, while NiA cells remain unaffected.

(**C**) A wing disc ablated with *DC^{GluR1}>>egr^{RNAi}* stained for DCP1 (gray) and Mmp1 (red). DAPI, blue. Both wound edge apoptotic cells and NiA cells remain unaffected by *egr* knockdown.

(**D**) A wing disc ablated with *DC^{GluR1}>>grnd^{RNAi}* and stained for DCP1 (gray) and Mmp1 (red). DAPI, blue. As in (**C**), both wound edge apoptotic cells and NiA cells remain unaffected following *grnd* knockdown.

(**E**) A wing disc ablated with *DC^{GluR1}>>rpr^{RNAi}* and stained for DCP1 (gray) and Mmp1 (red). DAPI, blue. Knockdown of *rpr* leads to a mild reduction of both wound edge apoptotic cells and NiA cells (open arrowheads).

(**F**) A wing disc ablated with *DC^{GluR1}* in a *hid^{1}* heterozygous background, and stained for DCP1 (gray) and Mmp1 (red), DAPI, blue. Both wound edge apoptotic cells and NiA cells are unaffected in this background.

(**G**) A wing imaginal disc ablated with *DC^{GluR1}>>miRHG* and stained for DCP1 (gray) and Nub (red). DAPI, blue. Tissue loss indicated by loss of Nub (arrowhead) is still observed

following ablation with *DC*^{GluR1} despite inhibition of apoptosis by knockdown of *rpr, hid,* and *grim.*

(**H**) Schematic of the *egr-Gal4 ; UAS-GFP* reporter showing activity in the adult muscle precursor cells (AMPs) just below the notum.

(**I-J**) Wing imaginal discs bearing an *egr* reporter (*egr-GAL4; UAS-GFP*, green) in an undamaged heat shocked disc (**I**) and following ablation with a version of *DC*^{GluR1} that lacks the *DVE>>GAL4* (**J**). DAPI, blue. Reporter activity is not observed in the pouch with or without ablation

Figure S5

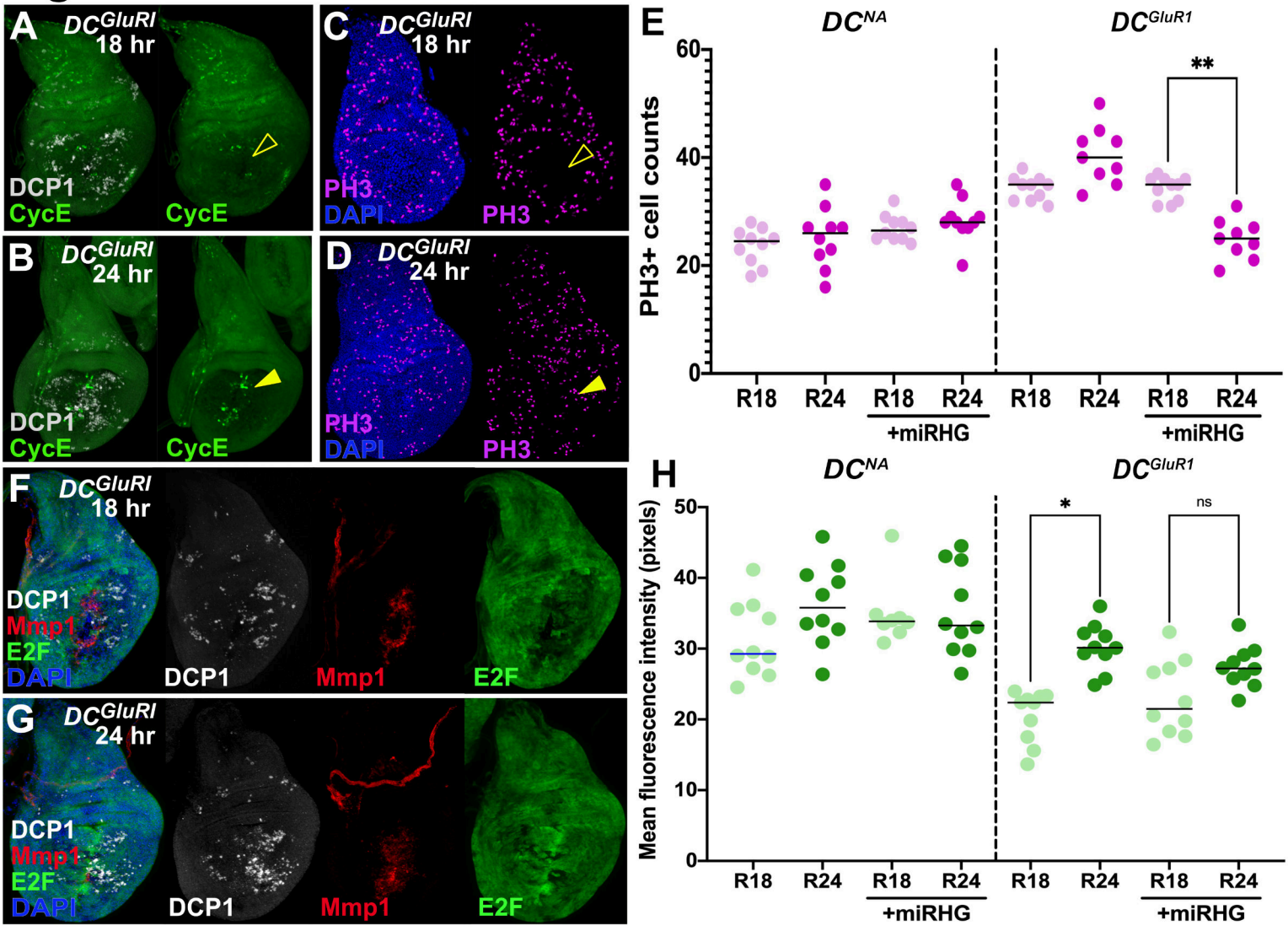
A
DCGluRI
18 hr
DCP1
CycE
CycE
B
DCGluRI
24 hr
DCP1
CycE
CycE
C
DCGluRI
18 hr
PH3
DAPI
PH3
D
DCGluRI
24 hr
PH3
DAPI
PH3
E
DCNA
DCGluR1
PH3+ cell counts
60
40
20
0
**
R18
R24
R18
R24
+miRHG
R18
R24
R18
R24
+miRHG
F
DCGluRI
18 hr
DCP1
Mmp1
E2F
DAPI
DCP1
Mmp1
E2F
G
DCGluRI
24 hr
DCP1
Mmp1
E2F
DAPI
DCP1
Mmp1
E2F
H
DCNA
DCGluR1
Mean fluorescence intensity (pixels)
50
40
30
20
10
0
*
ns
R18
R24
R18
R24
+miRHG
R18
R24
R18
R24
+miRHG

Figure S5. Related to Figure 6.

Quantification of proliferation with NiA manipulation.

(**A-B)** Wing imaginal discs bearing the *CycE-GFP* reporter (green) at 18 hr (**A**) and 24 hr (**B**) of recovery following ablation by DC^{GluR1} and stained for DCP1 (gray). DAPI, blue. The open arrowhead in (A) indicates a lack of reporter activity in the *salm* domain, while the arrowhead in (B) highlights stronger reporter activity at 24 hr.

(**C**-**D**) Wing imaginal discs after 18 hr (**C**) and 24 hr (**D**) of recovery following DC^{GluR1} ablation, and stained for DCP1 (gray), PH3 (magenta), and DAPI. The open arrowhead in (C) indicates a lack of PH3 in the *salm* domain, while the arrowhead in (D) highlights increased PH3 at 24 hr.

(**E**) Quantification of PH3+ cells in DC^{NA} disc and in DC^{GluR1} ablated discs, both in the presence and absence of *miRHG* and after 18 hr and 24 hr after the heat shock/recovery. P** < 0.005. Data was analyzed via a Kruskal-Wallis test and a Tukey's multiple comparisons test. n = 10 discs for each treatment.

(**F**-**G**) Wing discs bearing the *PCNA-GFP* reporter at 18 hr (**F**) and 24 hr (**G**) of recovery following DC^{GluR1} ablation, and stained for DCP1 (gray) and Mmp1 (red). DAPI, blue.

(**H**) Quantification of the mean fluorescence intensity of the *PCNA-GFP* signal at 18 hr and 24 hr of recovery in the presence and absence of *miRHG*, following DC^{GluR1} ablation. ns. P* < 0.0445. Data was analyzed via a Kruskal-Wallis test and a Tukey's multiple comparisons test. n = 10 discs for each treatment.